Received: 25 May 2021 | Revised: 11 January 2022 | Accepted: 14 February 2022

DOI: 10.1002/eqe.3627

RESEARCH ARTICLE

WILEY

Seismic analysis of a modern 14-story reinforced concrete core wall building system using the BTM-shell methodology

Marios Mavros[1] | **Marios Panagiotou**[2] | **Ioannis Koutromanos**[3] | **Rodolfo Alvarez**[4] | **Jose I. Restrepo**[5]

[1]Department of Civil and Environmental Engineering, University of Cyprus, Nicosia, Cyprus

[2]Nabih Youssef Structural Engineers, Los Angeles, California, USA

[3]Department of Civil and Environmental Engineering, Virginia Polytechnic Institute and State University, Blacksburg, Virginia, USA

[4]MM Engineers SC, Mexicali, Baja California, México

[5]Department of Structural Engineering, University of California San Diego, La Jolla, California, USA

Correspondence
Marios Mavros, Department of Civil and Environmental Engineering, University of Cyprus, Nicosia, Cyprus.
Email: mavros.marios@ucy.ac.cy

Abstract

This paper uses computational simulation to investigate the lateral load-displacement behavior and failure modes of a modern 14-story reinforced concrete (RC) core wall building. The design complies with the minimum code requirements of the current California Building Code, which is based on ASCE 7–16 and ACI 318–14. The computational representation of the building, which accounts for the material nonlinearities of all structural components, employs the beam-truss model (BTM) for the walls and floor slabs. Analyses of the building model are conducted for static monotonic and cyclic lateral loads using the program FE-MultiPhys, which provides a user-friendly implementation of the BTM as an assemblage of rectangular shell macroelements. Two different load patterns, that is, lateral load distributions along the building height, are considered. The analyses provide insights into the evolution of damage and lateral strength degradation and their dependence on the load pattern, while also elucidating the complex interaction between the webs and flanges of the core wall and the system effects associated with coupling between the walls, beams, slabs, and columns. The presentation of the analytical results is accompanied by a discussion on the advantages of the BTM over seismic analysis methods used in current code-minimum and performance-based seismic design (PBSD) practice.

KEYWORDS

flexure-shear interaction, nonlinear analysis, performance-based seismic design, reinforced concrete buildings, seismic design, structural flanged coupled core walls, structural seismic damage, system effects

1 | INTRODUCTION

Reinforced concrete structural walls (RCSW) are the most common structural system for medium- and high-rise buildings in many regions of high seismicity, such as the West Coast of the US, Chile, and New Zealand. The majority of modern RCSW buildings with ten or more stories uses nonplanar flanged walls, such as C-shape walls. Well-proportioned and detailed RCSW provide high lateral stiffness and strength, which result in efficient seismic drift control. Seismic design provisions for RCSW include design and detailing requirements to ensure the development of inelastic deformations in

targeted regions, termed plastic hinges, located typically in the vicinity of the walls' base. For RCSW buildings up to 73 m (240 ft) high that are located on a Seismic Design Category D or E, the ASCE 7–16 document [1] allows the use of response spectrum analysis, a response modification coefficient $R = 6$, and a deflection amplification factor $C_d = 5$. The analysis is conducted on a building model which uses effective stiffness for the various members.

A key seismic design parameter of RCSW buildings is the shear stress in each wall. The ACI 318–14[2] document, requires that the factored shear stress of individual wall piers shall not exceed $0.5\sqrt{f'_c}$ MPa ($6\sqrt{f'_c}$ psi), with a strength reduction factor φ equal to 0.6 for cases where capacity design is not conducted. The corresponding limit value for the average shear stress of all wall webs aligned with a particular direction is $0.4\sqrt{f'_c}$ MPa ($4.8\sqrt{f'_c}$ psi). The shear stress is calculated using the design earthquake forces, which are two thirds of the forces calculated for the risk-targeted Maximum Considered Earthquake ($\mathrm{MCE_R}$). If the lateral forces are calculated via a modal response spectrum analysis procedure, the base shear cannot be taken less than that calculated from the equivalent lateral force procedure.

For buildings taller than 73 m (240 ft), RCSW is permitted as an *Alternative Structural System* after an independent review and approval of the structural design by the local jurisdiction. The design review requires the use of nonlinear response history analysis to verify that the probability of collapse, conditioned on the occurrence of the $\mathrm{MCE_R}$ intensity, is less than 10%. The analysis and analytical design verification of such buildings typically follow the performance-based seismic design (PBSD) guidelines of the Los Angeles Tall Buildings Structural Design Council (LATBSDC)[3] or of the Tall Buildings Initiative (TBI)[4] by the Pacific Earthquake Engineering Research Center (PEER). The same guidelines can be used for RCSW buildings with a height lower than 73 m (240-ft) which are designed for a superior performance than that implied in the design codes.

The PBSD practice does not involve an explicit calculation of the collapse probability. Instead, the requirement for a sufficiently low probability of collapse is considered satisfied by ensuring that several criteria, provided in the guidelines, are met. For instance, the LATBSDC[3] guidelines stipulate that an acceptable design is attained, if 1.5 times the average shear stress on the walls, obtained for a collection of eleven ground motions scaled to the $\mathrm{MCE_R}$ intensity, does not exceed a limiting stress. The factored shear stress limit ranges between $0.62\sqrt{f'_{ce}}$ MPa ($7.5\sqrt{f'_{ce}}$ psi) and $0.83\sqrt{f'_{ce}}$ MPa ($10\sqrt{f'_{ce}}$ psi), where $\varphi = 0.75$ and f'_{ce} is the expected compressive strength of the concrete. The exact value of limiting shear stress depends on the analytically obtained average tensile and compressive strains in the plastic hinge regions of the walls. The shear stress acceptance criteria of the LATBSDC[3] have been based on statistical analysis (Wallace et al.[5]) of experimental tests of RCSW components. The validity of these criteria for buildings using coupled C-walls may be limited for several reasons. First, the available experimental dataset includes one test on coupled C-walls, reported by Barbachyn et al.[6] This specimen may not be representative of the typical detailing or seismic demands of multistory walls, as it included partially post-tensioned coupling beams. Furthermore, that specimen was subjected to a lateral force distribution corresponding to the first mode of dynamic response, which led to relatively low values of peak shear stress in the walls, equal to $0.25\sqrt{f'_{ce}}$ MPa ($3\sqrt{f'_{ce}}$ psi). Second there are only two tests on C-shape walls under multiaxial loading, namely, the tests by Beyer et al.,[7] wherein the peak in-plane wall shear stress values were equal to $0.46\sqrt{f'_{ce}}$ MPa ($5.5\sqrt{f'_{ce}}$ psi). This also happens to be the largest value of shear stress reached for a T-shaped wall tested under uniaxial loading (Thomsen and Wallace[8]). The only walls in the dataset for which the shear stress exceed a value of $0.62\sqrt{f'_{ce}}$ MPa ($7.5\sqrt{f'_{ce}}$ psi) were subjected to unidirectional loading and had a barbell or H-shape section which are fundamentally different from a coupled flanged core wall. Based on the above, it is necessary to investigate the levels of shear stress that can be carried by RCSW flanged coupled walls and determine whether the limit shear stress values in design standards and guidelines are adequate. Experimental testing is the most reliable type of investigation, but it is not feasible to conduct parametric experimental investigations of entire building systems which accurately reproduce the load and deformation conditions of core walls. Thus, computational simulation must be employed to provide insights on the internal forces, deformations, shear stresses and failure modes, and enable the verification of PBSD guidelines.

The nonlinear analysis of RCSW buildings for PBSD typically relies on RC wall panel elements with a fiber-section model to account for the nonlinear in-plane axial-flexure interaction. RC wall panel element formulations are available in commercial software employed for PBSD in the US, such as PERFORM3D.[9] The elements in PERFORM3D use a single integration point, which enforces constant strains along the length of the element, and they describe the sectional force-deformation behavior through a fiber sectional model. The out-of-plane bending moment and shear resistance are assumed to be linearly elastic, and the cracked stiffness properties used (LATBSDC[3]) are independent of the mechanical characteristics of the sections (e.g., flexural steel ratio, axial load ratio, etc). Typically, one or two wall panel elements are used per story, aiming to empirically calibrated plastic hinge lengths.[3] The assumption of constant strains over each RC wall panel element is in contrast with experimental testing measurements and damage observations in earthquakes.[7,8,10–13] Wall panel elements that act as beam-based models do not accurately capture the nonlinear flexure-shear interaction that often controls the strength degradation and failure modes of ductile RCSWs as

explained in[14–19] Lu and Panagiotou[15] showed that using fiber section Euler–Bernoulli beam elements for the simulation of nonplanar walls results in significant overestimation of the stiffness and hysteretic energy dissipation. Similarly, coupling beams are modeled with empirically calibrated lumped-plasticity beam elements which do not account for flexure-shear interaction or for axial elongation effects between coupling beams and wall piers as demonstrated in Alvarez et al.[17] and Lu and Panagiotou.[20] Finally, the slab diaphragms are modeled as linear elastic, while the framing effects between walls, slabs, and columns are ignored for spans longer than 6.1 m (20 ft) (LATBSDC[3]).

Several studies have been dedicated to the finite element simulation of planar and nonplanar RC walls.[21–23] The continuum-based finite element modeling scheme by Palermo and Vecchio[21] was capable of capturing some aspects of the hysteretic behavior and failure modes for a set of experimentally tested walls. Dashti et al.[23] employed a similar modeling approach, which used geometrically nonlinear shell elements, capturing strength degradation due to global out-of-plane buckling. Moharrami and Koutromanos[22] employed a finite element approach using large-deformation kinematics, three-dimensional solid elements for the concrete material, and beam elements for the reinforcing steel. The employed constitutive models accounted for all damage modes in the concrete and reinforcing steel, including bar rupture. They employed their method to simulations of flexure-dominated planar and nonplanar walls that were experimentally tested and ultimately failed due to web crushing or vertical bar buckling and subsequent rupture in the boundary elements. None of the above methods have been validated for all failure modes of planar and flanged ductile walls, that is, bar buckling and rupture, crushing of concrete, diagonal tension failures, web horizontal crushing and sliding, vertical boundary-web interface failure, global out-of-plane plastic hinge buckling.

Simplified analysis models, tailored to the simulation of walls, have also been formulated and employed. The multiple vertical line element model (MVLEM)[24,25] has been used in simulations of coupled slender rectangular and flanged walls.[26] The method does not capture strength degradation of slender walls associated with shear failures, as it essentially enforces a plane-section kinematic constraint to the solution. Additionally, the method is not capable of capturing the impact of bar buckling and rupture. Furthermore, the method, for nonplanar walls,[24,26] uses a linearly elastic law to describe the out-of-plane flexural behavior of walls.

Recent studies have employed shell finite element models of three-dimensional RC wall building systems to elucidate the observed seismic damage in actual structures during the 2010 Maule, Chile earthquake. Vasquez et al.[27] investigated the dynamic response of an 18-story building that failed at a relatively low roof drift ratio of 0.34% due to vertical crushing at the base. They simulated the building using a nonlinear shell model and a hybrid model, which combined force-based beam elements with a fiber section for the components at the lower stories that exhibited nonlinearity, and elastic shell elements for the remaining components of the structure. Both models were shown to be capable of predicting compressive crushing associated with axial-flexure interaction. The study of Gallardo et al.[28] used nonlinear layered shell elements to model another 18-story building that incurred strength degradation at a story drift level of 0.2%, due to poor confinement of the concrete and inadequate protection of the vertical reinforcement against buckling. These models[27,28] assumed linearly elastic behavior for the floor slabs of the buildings. Additionally, the effect of buckling was either ignored at all or it was accounted for in an overly simplified fashion. Restrepo et al.[29] modeled the Alto Rio building that collapsed during the 2010 Maule earthquake using a model with four-node shell elements having embedded reinforcement bars. Their model was used in monotonic nonlinear static analyses and captured several aspects of the lateral strength degradation and collapse mechanism of the building. Finally, Maffei et al.[30] modeled the Alto Rio building using shell elements and reproduced the damage and strength degradation associated with crushing of unconfined regions. Shell-based finite element models can provide insights on the system-level performance and flexure-dominated failure modes, but their accuracy in capturing shear-dominated damage patterns may not be as good. For instance, Gallardo et al.[28] conducted a set of validation analyses for their modeling scheme using data of experimental tests on planar walls. They found that their model was very accurate for three flexure-dominated walls, but it was less accurate in the case of a wall that had exhibited shear failure in the form of extensive web crushing. Additionally, continuum-based finite element models may not be well-suited for capturing strongly localized cracks associated with nonlinear flexure-shear interaction and diagonal tensile failures in the walls due to the so-called locked-in stress effect.[31]

A powerful, algorithmically efficient alternative for simulation of structural walls under earthquake loading is the beam-truss model (BTM) by Lu et al.,[20,32] which allows the simulation of nonplanar walls and other components such as coupling beams and slabs. The BTM represents a RC component (wall, beam, and slab) with an assemblage of line elements and relies on uniaxial constitutive laws. Thus, it is conceptually simpler and algorithmically more efficient than finite element models. It is also advantageous compared to other simplified methods, as it does not enforce a plane-section condition and can explicitly model the nonlinear-flexure-shear interaction at any region of the mesh. The BTM has been shown to capture all common shear-flexure failure modes, such as diagonal tension and compression as well as horizontal and vertical web crushing of rectangular and flanged walls.[32] A recent study focusing on planar walls[19] also validated the

capability of the method to account for bar buckling, bar rupture and vertical crushing failure modes. It has also been used in simulations of RC slabs and even case studies of failure in multistory building systems under dynamic loads,[16] including a collapse simulation of the Alto Rio building.[33] Recent studies have also shown that the method can capture the cyclic behavior of coupled walls[17,18,20] and the out-of-plane inelastic buckling [34] Finally, the effect of lateral force profile on the deformation capacity of a core wall and the effect of the out-of-plane shear strength of the flanges of a core wall was studied in Alvarez[35] for monotonic static loading.

The present study employs computational simulation to enhance the understanding of the seismic performance of multistory RCSW buildings with coupled, C-shaped walls. The focus of the study is a 14-story RC core wall building located in downtown Los Angeles, designed in an earlier study (Alvarez[35]) according to the current California Building Code[36] which is based on ASCE 7–16[1] and ACI 318–14[2] documents. The simulations rely on the BTM to model the core wall and floor slabs, and beam elements for modeling the columns. The constitutive laws for concrete and reinforcing steel are capable of accounting for all important material damage modes, including bar buckling and rupture. Analyses are conducted for static monotonic and cyclic loads, considering different load patterns, that is, lateral force distributions along the height of the building. The analyses provide insights into the dependence of the system lateral strength and failure mode on the lateral load pattern, and the significant effect of nonlinear-flexure-shear-interaction on the evolution of damage and on the failure modes. System-level effects, associated with coupling between the core wall, the slabs, and the columns, and the impact of cyclic loading are also studied. Given the complexity of the nonlinear response of full building systems, due to nonlinear flexure-shear-interaction in the coupled flanged walls and their coupling with the slabs and columns, nonlinear static analyses with two simple load patterns are selected to analyze the building. Hence, any further complexity in evaluation and analysis of the results that would emerge from multiaxial and multimodal response is eliminated. Furthermore, this type of analysis yields results which can be directly compared to available data from static experimental tests. For these reasons, static nonlinear analyses are deemed appropriate in this study and not to replace any of the most accurate level of response and design validation that dynamic analysis offers.

2 | BUILDING DESCRIPTION

The focus of the analytical study is a hypothetical 14-story RC core wall building, located in downtown Los Angeles, California (34.05° N, 118.26° W). The configuration and reinforcing details of the building are presented in Figure 1. The figure also establishes a set of coordinate axes, X, Y, and Z, such that the sides of the floors are aligned with the first two axes, and the third axis is aligned with the height of the building, as shown in Figures 1A and 1B. The floors consist of 203 mm (8 in.) thick post-tensioned RC flat slabs, having a square plan configuration with a dimension of 28 m (92 ft). All stories have a height of 3.66 m (12 ft), and the total building height H is 51.2 m (168 ft). The core wall consists of two C-shaped walls, such that the wall webs (for X-direction loading) are configured as coupled piers along the X-direction as shown in Figure 1A and as solid walls along the Y-direction. The plan view of the building is shown in Figure 1B. Coupling in the X-direction is provided by 1016 mm (40 in.) deep beams as shown in Figure 1C. The core wall is 7.0 m (23 ft) long in the X-direction (each wall pier is 3.5 m [11.5 ft] long) and 7.9 m (26 ft) long in the Y direction. The thickness of the wall and coupling beams is equal to 610 mm (24 in.) for the bottom five stories, and 508 mm (20 in.) for all other stories. The cross-sectional dimension of the columns is 600 mm (23.6 in.) as shown in Figure 1D. The total seismic weight, W, of the building consists of the self-weight and 1.92 kPa (40 psf) superimposed dead loads and is equal to 93.5 MN (21,020 kip).

3 | BUILDING DESIGN

The building, described in detail in Alvarez,[35] was made of concrete having a specified compressive strength, f'_c, of 48.3 MPa (7 ksi) for the walls and columns, and of 34.5 MPa (5 ksi) for the slabs, and Grade 60, ASTM 615 reinforcing steel with a nominal yield strength, f_y, of 414 MPa (60 ksi). The seismic design used response spectrum analysis for a Site Class D, Risk Category II, and the spectral parameters S_{DS} and S_{D1} were equal 1.31 and 0.79 g, respectively. The seismic response modification coefficient R was taken equal to 6, and the redundancy factor ρ was set equal to 1.3, following the minimum base-shear requirements of ASCE 7–16 that control the design. The calculation of the design actions was conducted using the program *ETABS Ultimate* 18.0.2,[37] and the analytical model included the structure above the ground, idealized as fully fixed at the base. The walls and floor slabs were simulated with RC wall panel elements, whereas the columns and coupling beams were modeled with beam elements. The effective moment of inertia of the walls and beams

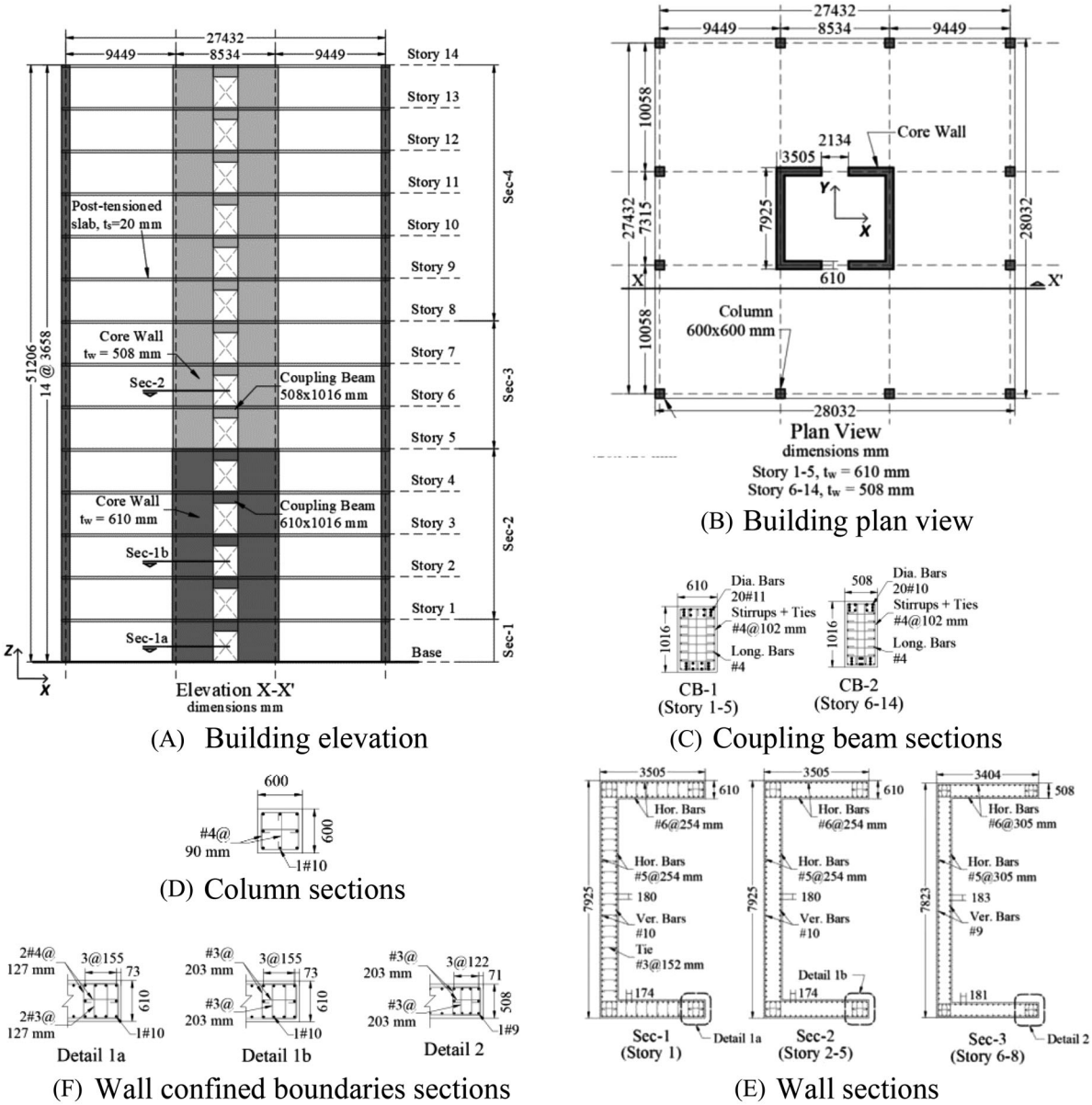

FIGURE 1 Geometry and section details of the building (Alvarez[35])

was taken equal to 0.5 and $0.3I_g$, respectively, where I_g is the gross section moment of inertia, per the guidelines of ACI 318–14.[2] The flexural stiffness of columns and slabs was neglected. The natural periods of the first translational modes along the X- and Y- direction were $T_{1X} = 1.39$ and $T_{1Y} = 1.49$ s, respectively. The design base shear force was 12.4 MN (2788 kip), corresponding to a design base shear coefficient, C_s, of 0.13.

The flexural design of the walls was controlled by the earthquake loading in the X-direction, which resulted in axial tension forces in one of the two C-shaped walls. The detailing scheme of the core wall considered four parts along the height of the building. The first part included the bottom story, and the second part included stories 2–5. The first two parts used a thickness of 610 mm and a longitudinal steel ratio, ρ_l, of 1.63% for the wall section. The third part included stories 6–8 and had $\rho_l = 1.54\%$, whereas the fourth part, which included stories 9–14, had $\rho_l = 1.21\%$. Both third and fourth parts used a thickness of 508 mm for the wall section. The wall sections and the reinforcing details of the first three parts are shown in Figure 1E. Special boundary elements, in accordance with the pertinent requirements of ACI 318–14,[2] were designed in the corner regions of the wall section, as shown in Figure 1F. The wall section outside the boundary elements at the bottom story included alternate anti-buckling #3 ties at a spacing of 152 mm, which is not a minimum code requirement but constitutes best practice.

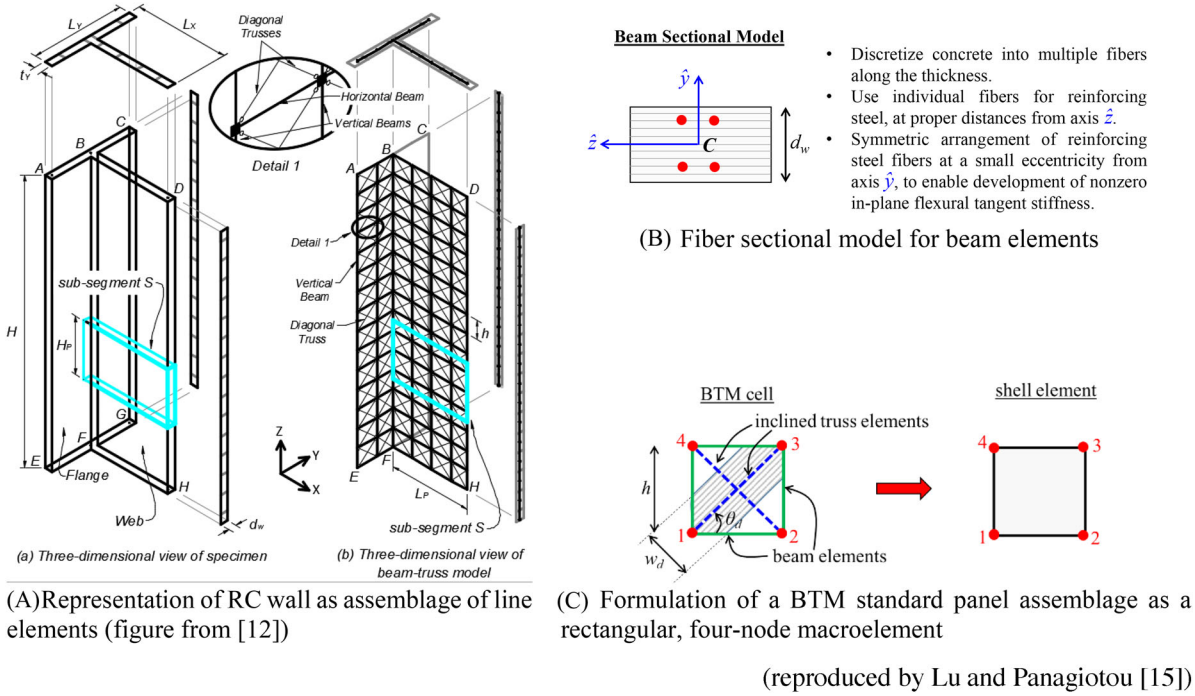

(A)Representation of RC wall as assemblage of line elements (figure from [12])

(B) Fiber sectional model for beam elements

(C) Formulation of a BTM standard panel assemblage as a rectangular, four-node macroelement

(reproduced by Lu and Panagiotou [15])

FIGURE 2 Beam–Truss Model (BTM) and implementation

The wall shear stress design demand values in the X- and Y-direction were $0.21\sqrt{f'_c}$ MPa ($2.53\sqrt{f'_c}$ psi) and $0.18\sqrt{f'_c}$ MPa ($2.17\sqrt{f'_c}$ psi), respectively, which were less than 50% of the shear stress limits in the ACI 318–14 building code.[2] The horizontal steel reinforcement ratio provided in the X- and Y- directions was $\rho_h = 0.37\%$ and 0.26%, respectively, for all stories. The unfactored nominal shear strength, V_n, of the core wall per ACI 318–14[2] was 22.9 MN (5148 kip) and 21.4 MN (4811 kip), corresponding to shear stresses of $0.39\sqrt{f'_c}$ MPa ($4.7\sqrt{f'_c}$ psi), and $0.32\sqrt{f'_c}$ MPa ($3.85\sqrt{f'_c}$ psi) for the X- and Y- direction, respectively. The shear demand-to-(unfactored) capacity ratio (DCR) was equal to 0.54 for the X-direction and 0.56 for the Y-direction.

Each coupling beam was provided with diagonal reinforcement and was fully confined along its length, as shown in Figure 1C. The coupling beams at the bottom five stories had 20 #11 bars and an unfactored nominal shear strength, V_n, of $0.83\sqrt{f'_c}A_{cv}$ MPa ($10\sqrt{f'_c}A_{cv}$ psi) while the beams at other stories were reinforced with 20 #10 bars and a shear strength of $0.81\sqrt{f'_c}A_{cv}$ MPa ($9.75\sqrt{f'_c}A_{cv}$ psi). The design shear demand was equal to $0.57\sqrt{f'_c}A_{cv}$ MPa ($6.86\sqrt{f'_c}A_{cv}$ psi). The columns were designed according to ACI 318–14[2] resulting to a longitudinal reinforcement ratio of 1.8% and a confining reinforcement volumetric ratio of 1.74%. The cross-section of the columns is shown in Figure 1D. Finally, each floor slab has a longitudinal steel ratio of 0.66% in both directions (0.33% at the top and 0.33% at the bottom) and is post-tensioned with 0.5 in. unbonded strands spaced at 304 mm (1 ft) in both directions, with an effective post-tensioning force of 120 kN (27 kips).

4 | ANALYSIS METHODOLOGY

The computational simulation of the building relies on the beam-truss-model (BTM) methodology described in detail in Lu and Panagiotou[20] and Lu et al.[32] The specific approach is deemed ideal for the analysis of seismic response and failure of RCSW buildings, as it combines accuracy with conceptual simplicity and computational efficiency. As schematically summarized in Figure 2A, the BTM uses an assemblage of horizontal and vertical beam elements and inclined truss elements to represent a wall, beam, or slab component. The diagonal truss elements are aimed to represent the inclined in-plane compression field of RC components. The beam elements include a fiber sectional model, wherein the cross-sectional dimension along the thickness of the member is subdivided into multiple fibers, each having its own stress-strain (constitutive) law, as shown in Figure 2B. The figure also presents the local cross-sectional axes, $\hat{y}$ and $\hat{z}$, for the beam element, such that axis $\hat{y}$ is aligned with the thickness of the wall. A fiber sectional model allows to describe the nonlinear

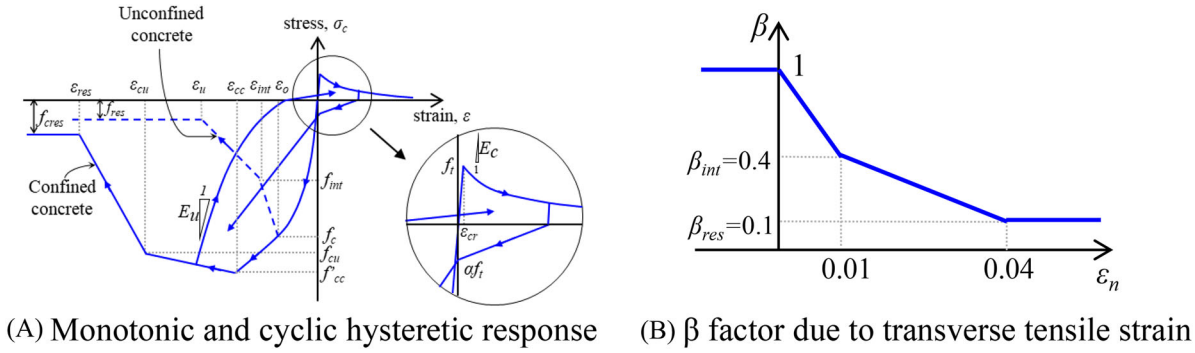

FIGURE 3 Behavior of concrete materials (reproduced by Lu and Panagiotou[15])

out-of-plane flexural resistance of the planar concrete component, while using uniaxial material laws for the concrete and reinforcing steel. For in-plane loading, the beam elements essentially behave as trusses, that is, they can only develop axial resistance. A very small but non-zero in-plane flexural stiffness is provided in the beam elements, by symmetrically arranging the reinforcing steel about the origin of the local sectional axes, so that the different fibers representing the steel are spaced apart by a distance of 2 mm in the $\hat{z}$-axis. This very small flexural resistance is introduced to prevent the occurrence of problems associated with singularity of the tangent stiffness matrix in an analysis.

A potential challenge associated with the use of the BTM by professional engineers for analysis of three-dimensional, multistory buildings, is the need to create a line-elements assemblage to represent the nonplanar walls and the floor slabs. To facilitate the use of the BTM for such cases, the present study employs a user-friendly implementation of the method which is available in the finite element program FE-MultiPhys.[38] In this implementation, a BTM cell, consisting of four nodes arranged as the corners of a rectangle and interconnected with two horizontal beam elements, two vertical beam elements and two inclined truss elements, has been programmed as a rectangular shell macroelement, termed BTM-shell,[39] as schematically shown in Figure 2C. This approach substantially simplifies the pre-processing and post-processing stages of an analysis, while still maintaining the predictive capabilities of the BTM as a simulation tool.

A key parameter for a BTM representation of a RCSW component is the inclination angle, θ_d, of the truss elements, as shown in Figure 2C. The value of θ_d in the present study is set equal to 62° and has been calculated in Alvarez[35] using the method described in Lu and Panagiotou.[15] The specific method is based on the plastic truss theory, combined with the assumption that the peak in-plane shear force of a planar RC wall component is entirely resisted by the horizontal reinforcing steel parallel to the direction of loading. After obtaining the value of θ_d, the cross-sectional width of the truss elements, w_d, can be obtained using the relation $w_d = h \cdot \cos(\theta_d)$, where h is the length of the vertical beam elements in the BTM representation, as shown in Figure 2C. This sectional width is then multiplied by the thickness of the component to give the cross-sectional area of the diagonal truss elements.

5 | MATERIAL MODELS

The uniaxial constitutive law for concrete is schematically summarized in Figure 3A and has been originally formulated by Lu and Panagiotou.[15] The specific material model accounts for strength and stiffness degradation associated with tensile cracking and compressive crushing. It also accounts for the increased compressive strength and ductility of confined concrete. As shown in Figure 3A, compressive strength degradation for unconfined and confined concrete occurs when the magnitude of the strain exceeds a threshold value equal to ε_o and ε_{cc}, respectively. After this point, the concrete exhibits softening, until it reaches a strain value equal to ε_u and ε_{res}, respectively. The value of the material parameters for confined concrete is obtained using the equations by Mander et al.[40] Softening in the post-crack tensile strain regime is described by an exponential curve. For the diagonal truss elements, the concrete constitutive law accounts for the effect of normal tensile strain, ε_n, on the compressive resistance, in accordance with the work of Vecchio and Collins.[41] Specifically, compressive axial stresses for the truss elements are multiplied by a reduction coefficient, β, which expresses the effect of normal tension on the compressive stress of concrete. The value of β depends on the normal tensile strain of each truss element following the law presented in Figure 3B. The value of ε_n for each diagonal truss element is obtained by first calculating an in-plane (membrane) strain tensor at the centroid of the BTM shell element, using the shape functions

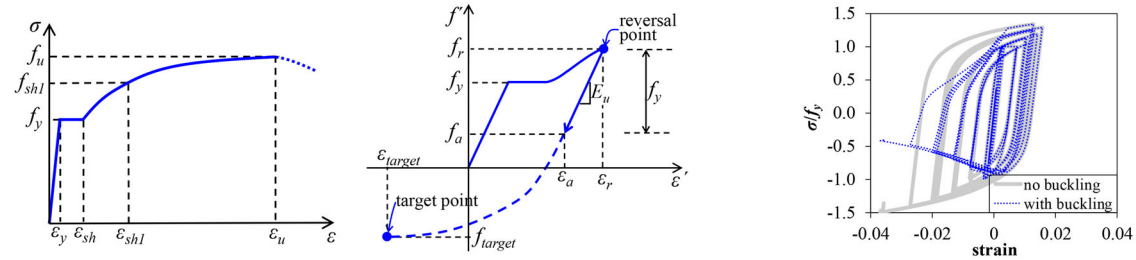

(A) Monotonic tensile response (B) Cyclic hysteretic response (C) Impact of buckling on cyclic hysteretic response (figure from Girgin et al. [44])

FIGURE 4 Behavior of reinforcing steel material

of a four-node quadrilateral finite element and the in-plane nodal displacements, and then obtaining the projection of the in-plane strain tensor in the direction normal to that of the truss element. A mathematically equivalent approach for calculating the normal strain has also been used in Lu et al.[32]

Since the stress-strain relations, schematically shown in Figure 3A, include softening, it is necessary to ensure that the analysis scheme is not affected by spurious mesh-size effects associated with strain localization. This is accomplished through use of the regularization scheme presented in Lu and Panagiotou,[15] which is based on the stipulation that the stress-strain laws, defined for the material of the truss elements, correspond to an element whose length is equal to a reference length value, L_{ref}. If the actual element length L is different than L_{ref}, then the parameters (ε_u, ε_{cint}, ε_{cu}) of the softening branch are adjusted to ensure that the amount of energy dissipated in the softening process is independent of the element length L. For unconfined concrete, the reference length value, L_{ref}, is set equal to 600 mm (23.6 in.) for the horizontal and vertical truss elements, and equal to 850 mm (33.5 in.) for the inclined elements. The specific values of L_{ref} were established by Lu and Panagiotou,[15] based on the length of the sides and diagonals of the unconfined concrete panels used in the study by Vecchio and Collins.[41] For confined concrete, the value of L_{ref} is set equal to 450 mm (17.7 in.), as this was the gauge length used to calculate strains in the concrete cylinders tested in the work of Mander et al.[40]

The reinforcing steel material is described by the uniaxial constitutive law proposed by Kim and Koutromanos.[42] This law represents the hysteretic stress-strain behavior using the equations previously proposed by Dodd and Restrepo[43] and a non-iterative stress-update algorithm. As opposed to steel models used in earlier studies employing nonlinear truss models, this steel law has the capability to account for the effect of buckling and rupture due to cyclic inelastic loading. It has been successfully used in simulations involving both refined finite element models[22] and simplified, beam-based models.[44] In the absence of buckling or rupture, the material model is fully calibrated using the monotonic stress-strain behavior, shown in Figure 4A. The constitutive model includes a hysteretic law to capture the cyclic response of reinforcing steel, as schematically shown in Figure 4B. Buckling is modeled using a criterion defined in terms of axial stress, proposed in Kim and Koutromanos.[42] A schematic comparison of hysteretic stress-strain response with and without modeling buckling is provided in Figure 4C.

The buckling criterion and the law to account for the buckling effect on the axial stress require the calibration of an additional slenderness parameter, L/d, defined as the ratio of the bar segment that buckles over the diameter d of the bar. For reinforced concrete (RC) members, the value of L/d can be defined using a procedure proposed by Dhakal and Maekawa,[45] shown by Girgin et al.[44] to be capable of accurately describing the occurrence of buckling in RC members subjected to cyclic loads. The bar rupture under cyclic strain histories is accounted for through a criterion based on the evolution of a quantity D which is related to the inelastic work accumulated under tensile stress. Specifically, given the true material stress, f, and the plastic strain rate, $\dot{\varepsilon}_p$, the evolution of D is governed by the following equation:

$$\dot{D} = \begin{cases} \left(\frac{f}{f_y}\right)^{2t} \dot{\varepsilon}_p, \text{if } f > 0 \\ 0 \qquad\qquad \text{otherwise} \end{cases} \tag{1}$$

where f_y is the yield stress and t is a material constant. Material failure, that is, rupture, occurs when the value of D becomes equal to D_{cr}, which is also a parameter of the material model. Once the rupture criterion is met at a location of a wall, the material model is rendered incapable of developing any resistance for the remainder of the loading process.

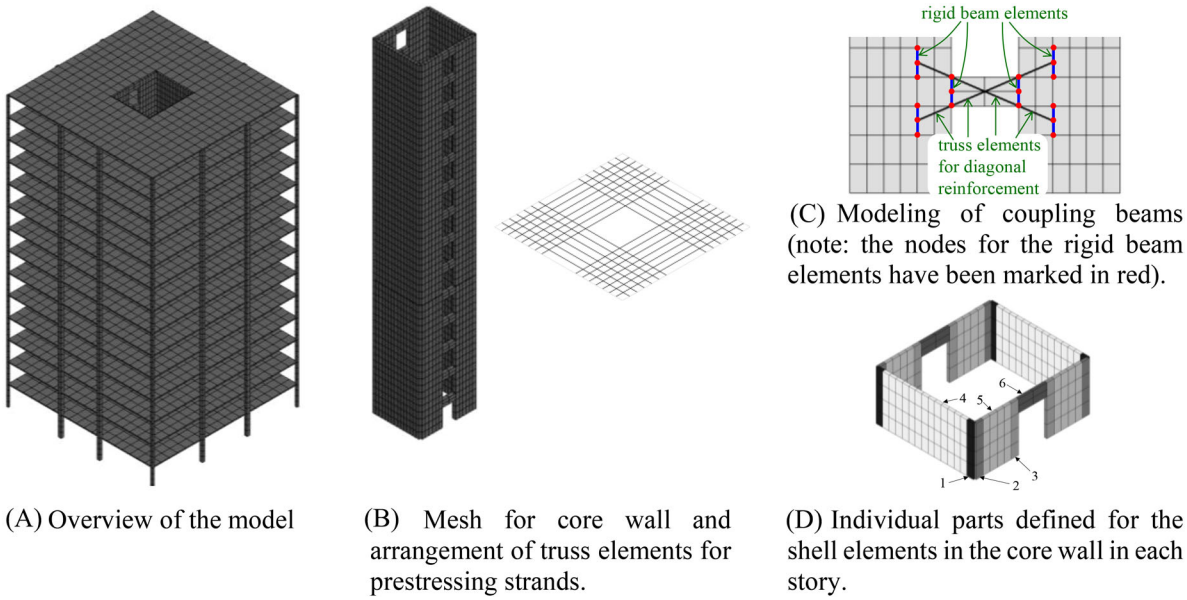

(A) Overview of the model

(B) Mesh for core wall and arrangement of truss elements for prestressing strands.

(C) Modeling of coupling beams (note: the nodes for the rigid beam elements have been marked in red).

(D) Individual parts defined for the shell elements in the core wall in each story.

FIGURE 5 Computational model for the building

6 | ACCOUNTING FOR NONLINEAR OUT-OF-PLANE SHEAR BEHAVIOR OF RC WALL PIERS

An enhancement made to the BTM methodology in the present study is aimed to improve the accuracy of the method in modeling the out-of-plane shear capacity of RC wall piers (flanges). This enhancement is necessary to avoid the spurious development of lateral reserve capacity from the flanges of a wall. The present study enforces an upper bound (cap) to the value of out-of-plane shear forces that can develop in the vertical beam elements of a BTM model. Specifically, the shear force of these elements along the thickness direction, that is, along the local $\hat{y}$-axis of the beam section in Figure 2B, is not allowed to exceed a user-specified value, V_r. The value of V_r for each vertical beam element is set equal to the nominal shear capacity obtained by the shear design provisions of ACI 318–14,[2] based on the element reinforcement and cross-sectional dimensions. The nominal shear capacity of the vertical beam elements in the confined boundary regions of the walls is calculated by considering these elements as columns.

The cap to the out-of-plane shear capacity for each vertical beam element is enforced in a computation by considering the nodal force component $\hat{V}$ along the local$\hat{y}$-axis shown in Figure 2B. If the magnitude of $\hat{V}$ exceeds V_r, then the force component of each node along the local $\hat{y}$-axis is multiplied by a reduction coefficient which is equal to $|V_r/\hat{V}|$. The same reduction coefficient is applied to the two nodal moment components about the local $\hat{z}$-axis shown in Figure 2B, to ensure that each beam element, as a whole, satisfies moment equilibrium after enforcing the shear-force cap.

7 | BUILDING MODEL AND ANALYSIS SETUP

The computational model for the building is depicted in Figure 5A, and the part of the BTM-shell element mesh representing the core wall is shown in Figure 5B. The unbonded post-tensioning strands are modeled with truss elements which is attached at opposite edges of the floor slab without any connection to the interior nodes of the slab with the strands' layout shown in Figure 5B. The column members are modeled with displacement-based beam elements, with four equally sized beam elements per story. The BTM shell elements representing the coupling beams have a finer size than the corresponding size of the BTM shell elements used for the wall along the height of the building, as shown in Figure 5C. As shown in the same figure, a set of rigid beam elements is used to ensure the displacement continuity across the interface between the regions with different element sizes. The diagonal reinforcing bars in the coupling beams are modeled with separate truss elements, as schematically shown in Figure 5C. This figure indicates that the end nodes of the truss element assemblages representing the diagonal bars do not coincide with nodal points of the BTM shell elements. For this reason, rigid beam elements are used to ensure the proper connection between the truss elements and the surrounding shell elements.

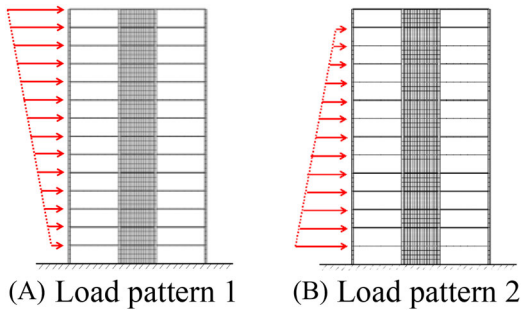

FIGURE 6 Lateral load patterns (distributions of force along height) considered in the analytical study

The plane of the BTM shells coincides with the mid-plane of each wall or slab. At the corners of the core wall, the BTM shell elements extend up to the centroid of the intersection of the two walls but at the free end of the wall the BTM shells extend up to the edge of the wall.

The model of the building uses 3136 elements for the core wall, 4368 elements for the floor slabs, 672 beam elements for the columns, 224 truss elements for the diagonal reinforcing bars and 420 elements for the post-tensioning tendons. The elements in the model are assigned to various parts, each part corresponding to different material and cross-sectional properties. A total of six parts are used for the BTM shell elements representing the core walls in each story, as shown in Figure 5D. The reinforcing steel content values ρ_l and ρ_t for the longitudinal and transverse direction, respectively, are summarized for these six parts in Table 1. The same table also provides the calibrated values of the out-of-plane shear strength, V_r, used for the web and flange regions of the wall. All BTM shell elements use six concrete fibers along the $\hat{y}$-axis and four steel fibers, as shown in Figure 2B. The beam elements of the columns use a 4 by 4 grid of concrete fibers and eight steel fibers at the locations of the longitudinal reinforcing bars. The model sectional discretization is verified through analysis, not shown in this study, that is, fine enough.

The analyses use expected values for the material strength parameters. The expected concrete compressive strength, equal to 1.3 times the corresponding specified strength, is 62.74 MPa (9.1 ksi) for the core walls and columns and 44.82 MPa (6.5 ksi) for the floor slabs. The remaining parameters that are required to fully define the monotonic stress-strain curve of the unconfined concrete, shown in Figure 3A, are assigned the values $\varepsilon_0 = 0.002$, $\varepsilon_u = 0.006$, $f_{int} = 15$ MPa, $f_{res} = 0.1 f'_c$, and $f_t = 0.33\sqrt{f'_c}$ (MPa). The yield stress f_y in the steel material law is set equal to 478 MPa, the ultimate stress f_u is 769 MPa, and the modulus of elasticity is $E_s = 200$ GPa. The remaining parameters of the steel material law, presented in Figure 4A and required to fully determine the monotonic tensile stress-strain curve, are assigned the values $\varepsilon_{sh} = 0.01$, $\varepsilon_{sh1} = 0.03$, $\varepsilon_u = 0.106$, and $f_{sh1} = 586$ MPa. Kim and Koutromanos[42] found that calibrating the value of D_{cr} such that monotonic tension gives rupture at the actual rupture strain of the bar gives accurate predictions of rupture instant for cyclic loading. The present study adopts a value of D_{cr} equal to 0.25, which corresponds to a monotonic tensile rupture strain of 0.10. Several parts in the model corresponded to regions where the concrete is confined with transverse ties and exhibited increased compressive strength and ductility. The amount of tie reinforcement for the specific parts is presented in Table 2. The same table provides the calibrated values of the concrete material law parameters for confined concrete. The parameter ε_{res} is set to $\varepsilon_{cu} + 0.001$, and the values of the latter parameter are shown in Table 2.

The loads applied on the building consist of the gravity loading on the floor slabs and the lateral forces along the X- or Y- direction of the building simulating the seismic loads. The prestressing force on the tendons is applied as an initial (self-induced) strain. The gravity and lateral loads are uniformly distributed over the plan of each floor. In each analysis, the seismic forces are applied as proportional loads, wherein the lateral forces are obtained as the product of a load factor (whose value changes during the analysis) and a given, constant load pattern vector, which describes the spatial distribution of seismic forces. The value of the load pattern depends on the Z-coordinate of a node, that is, the location of the node along the height of the building. Two different load patterns are considered in the present study. The first load pattern, shown in Figure 6A, corresponds to a so-called inverted triangular force distribution, wherein the magnitude of the load pattern is linearly proportional to the Z-coordinate. This means that the largest lateral forces are applied on the top slab of the building. The effective height corresponding to such a load pattern is equal to $0.67H$. The second load pattern, shown in Figure 6B, corresponds to a so-called triangular force distribution, wherein the magnitude of the lateral force is a linear function of the Z-coordinate, the value of lateral forces at the roof slab is zero, and the largest lateral forces are applied at the roof of the base story, that is, at the 1st floor of the building. This second load pattern corresponds to

TABLE 1 Sectional properties for the different parts used to model the core wall

Part number	1			2			3			4			5			6	
Stories	ρ_l (%)	ρ_t (%)	V_r (kN/m)	ρ_l (%)	ρ_t (%)	V_r (kN/m)	ρ_l (%)	ρ_t (%)	V_r (kN/m)	ρ_l (%)	ρ_t (%)	V_r (kN/m)	ρ_l (%)	ρ_t (%)	V_r (kN/m)	ρ_l (%)	ρ_t (%)
1	2.2	1.27	3280	2.2	1.35	3124	2.2	1.35	3124	1.49	0.26	1198	1.54	0.37	1218	0.45	1.02
2-5	2.2	0.49	577	2.2	0.54	703	2.2	0.54	703	1.49	0.26	848	1.54	0.37	858	0.45	1.02
6-14	2.5	0.53	472	2.5	0.58	575	2.5	0.58	575	1.39	0.26	660	1.4	0.37	780	0.49	0.98

Note: ρ_l is the longitudinal reinforcement ratio; ρ_t is the transverse reinforcement ratio; V_r is the out-of-plane shear strength for planar wall elements, reported as force per unit width of the BTM shell element. A value of V_r is not reported for Part 6, as this part corresponds to the coupling beams.

TABLE 2 Material parameters for confined concrete

Component and part	Stories	ρ_v (%)	f'_{cc} (MPa)	ε_{cc}	ε_{cu}	f_{cu} (MPa)
Core wall: Parts 1, 2 and 3	1	1.00	86.7	0.0058	0.0353	45.4
	2-5	0.29	70.2	0.0032	0.0161	20.3
	6-14	0.35	71.7	0.0034	0.0177	23.3
Core wall: Part 6 (Coupling Beams)	1-5	1.01	89.9	0.0063	0.0297	56.2
	6-14	0.99	88.9	0.0062	0.0302	53.9
Columns	All	0.70	80.9	0.0049	0.0296	36.9

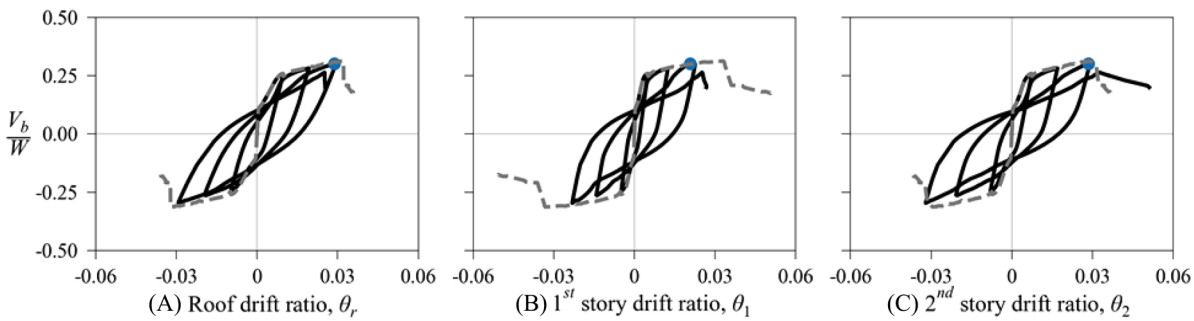

FIGURE 7 Hysteretic responses for loading along the X-axis using load pattern 1

an effective height of 0.33H and was selected to represent the effective height of the resultant lateral force obtained from nonlinear dynamic analysis of 10-, 15-, and 20-story tall core wall buildings subjected to Los Angeles MCE level of shaking as well as to unscaled near-fault ground motions.[46–48] Hence, load pattern 1 approximates a first mode dominated nonlinear dynamic response, while load pattern 2 represents nonlinear dynamic response with significant contribution of the higher modes.

The solution for the nonlinear analyses employs an incremental-iterative scheme. Initially, the gravity loads, and the prestressing of the tendons are applied in the model. Subsequently, the lateral loads are applied, and the solution at each step of the analysis is conducted through a displacement-control algorithm, using the horizontal displacement of a node located at the roof slab as the controlled degree-of-freedom. The analysis for each load pattern is conducted for monotonic and cyclic lateral loads. In the first case, the fixed values of controlled horizontal displacements are monotonically increased. The second case introduces a cyclic displacement history for each of the controlled displacements, and the amplitude of applied displacement is increased with each loading cycle. Separate analyses are conducted for seismic loads acting along the X- and Y-direction.

8 | ANALYSIS RESULTS

This section presents the analysis results for each of the two load patterns. The results for loading in the X-direction will be described first, followed by a presentation of the results for loading in the Y-direction.

8.1 | Results for loading in the X-direction

For loading in the X-direction, the lateral resistance of the structure is primarily contributed by the two coupled C-shaped walls, with most of the shear resistance being developed in the webs that have increased axial compression due to the coupling behavior (leading webs). The hysteretic curves, with the normalized base shear, V_b/W, as a function of the roof drift ratio, first-story ratio, and second-story ratio are shown in Figures 7 and 8, for load patterns 1 and 2, respectively. The roof drift ratio is defined as the ratio of roof lateral displacement over the height of the building. The point corresponding to the instant where the maximum base shear force is recorded is marked in each hysteretic plot. Figures 7 and 8 also

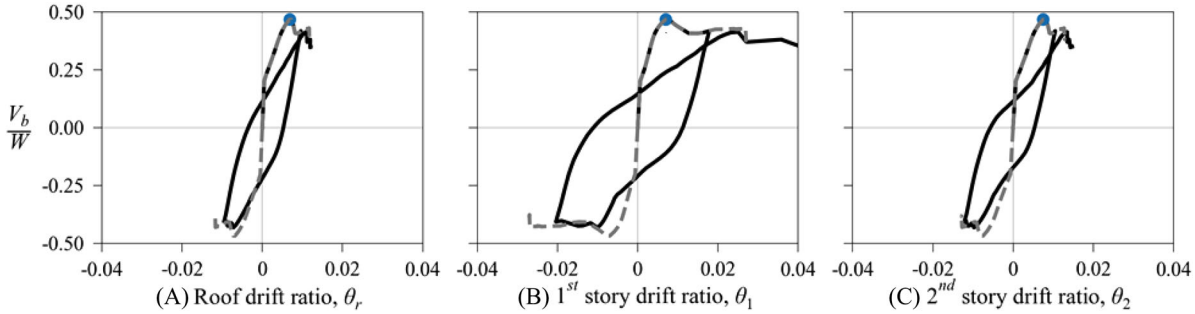

FIGURE 8 Hysteretic responses for loading along the X-axis using load pattern 2

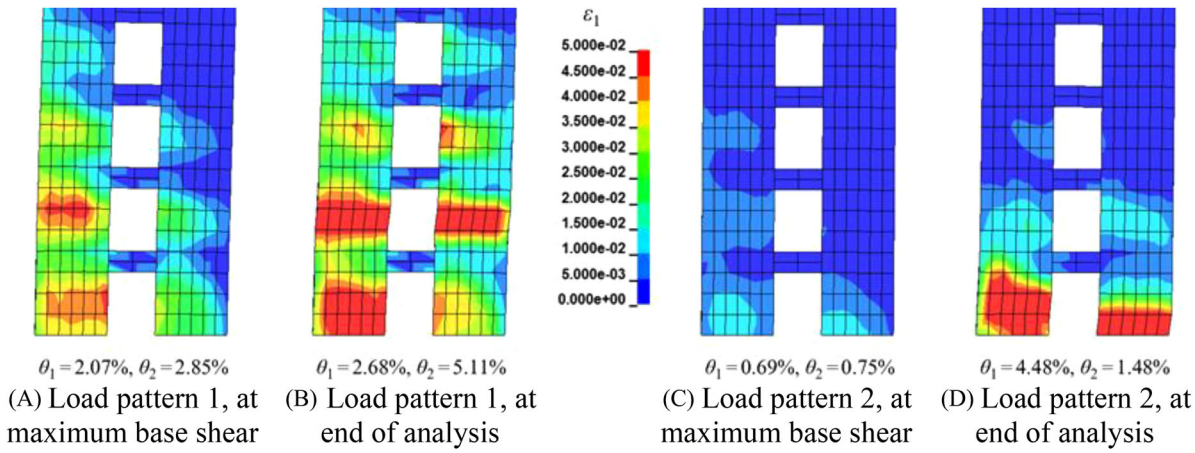

FIGURE 9 Deformed shape and max. principal strains (ε_1) of the core wall (X-elevation) for X-direction loading

include the corresponding curves obtained from monotonic analysis, which are generally found to match the envelope of the hysteretic curves before strength degradation. Under cyclic loading pattern 1, the structure sustained 2.93% roof drift and maximum base shear force ratio V_b/W of 0.3 before experiencing strength degradation. On the other hand, the maximum V_b/W for load pattern 2 is 0.47 and the drift capacity at the onset of strength degradation for load pattern 2 is 0.73%. The significantly lower drift capacity of the second load pattern is attributed to the larger plane shear stresses developed in the wall piers which in turn reduce their deformation capacity.

The elevations of the deformed shapes of the bottom five stories of the core wall together with the maximum principal strain contour plots, corresponding to the instant where the maximum base shear is obtained and to the end of the cyclic analysis, are shown in Figure 9. The figure also provides the story drift ratio, termed as to story drift from this point on, values at the bottom two stories corresponding to each plot. Strength degradation is caused by shear failure, and more specifically web crushing obtained in the second and the first story, for load patterns 1 and 2, respectively. The failure is manifested through the formation of bands with large values of maximum principal strain, as deduced from Figure 9.

The behavior obtained for load pattern 1 is highly ductile. The magnitude of drift reached prior to strength degradation is within the range of drift capacities that have been obtained in experimental tests of ductile full core walls[6] and C-shape walls.[7] The peak vertical tensile and compressive strains recorded in the wall up to the instant of peak base shear force are equal to 0.04 and 0.019, respectively. The peak compressive strain corresponds to significant local strength degradation for the confined concrete in the boundary elements, without any lateral strength degradation in the system. The behavior for load pattern 2 entails significantly lower inelastic deformability, with the peak wall tensile and compressive strains recorded up to the instant of peak base shear force being equal to 0.011, and 0.013, respectively. For load pattern 1, the two bottom stories carry similar shear forces, but the second story has a lower out-of-plane shear strength in the wall flanges, as deduced from Table 1. Consequently, the second story shear strength is lower than that of the bottom story, which explains why shear failure occurs in the second story when the structure is subjected to the first load pattern. For load pattern 2, the bottom story shear force is significantly higher than that of the second story. This explains why the second load pattern gives shear failure in the bottom story, despite the lower shear strength of the second story.

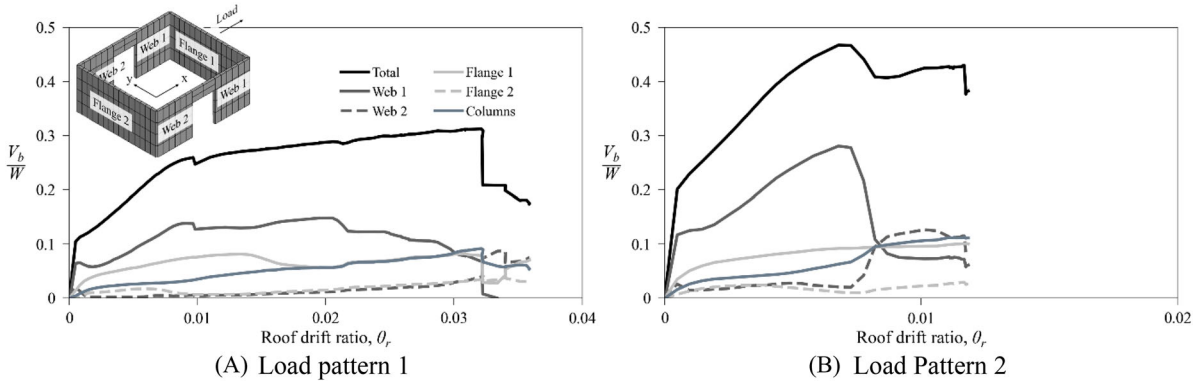

FIGURE 10 Contribution of various structural components to the lateral resistance of the structure, obtained for monotonic lateral loading along the X-direction

TABLE 3 Base shear contribution for cyclic loading along the X-direction at the instant of maximum base shear

Base shear contribution	Load pattern 1	Load pattern 2
Web 1	50%	60%
Web 2	7%	4%
Flange 1	22%	20%
Flange 2	9%	2%
Columns	12%	14%

Figures 10A and 10B provide the evolution of the lateral resistance contribution from the various components of the system, obtained from the monotonic analysis using load patterns 1 and 2, respectively. The figure distinguishes two web piers, termed web 1 and web 2. A similar distinction is made for the wall flanges. Web 1 and flange 1 correspond to the piers that will be subjected to a compressive axial force change due to the coupling action of the beams and slabs, while web 2 and flange 2 correspond to the piers that will experience a tensile axial force change because of coupling action. For both load patterns, the web 1 pier has a substantially higher contribution to lateral resistance than the other members, followed by flange 1. The web 2 and flange 2 piers have a practically negligible contribution in the pre-peak regime of response. The lateral system strength degradation is associated with diagonal crushing in web 1.

The contribution of the various elements to the base shear force resistance at the instant of peak base shear force for cyclic loading is listed in Table 3. It is worth noticing the minor resistance contribution of web 2, which does not exceed 7% for both load patterns. This value is entirely different than what would have been obtained by linear elastic analysis; the latter would result in similar shear force demands in all webs. This is a critical aspect of the behavior of coupled walls which has been studied by Panagiotou and Restrepo , [49] Panagiotou et al.,[13] Lu and Panagiotou[20] and Alvarez et al.[17,18] and cannot be captured by linear analysis. The coupling beam action introduces a vertical tension force on the wall C-segment 2, consisting of webs 2 and flange 2, while an increased vertical compression force is imposed to C-segment 1, consisting of webs 1 and flange 1. For example, at the instant of peak base shear force for load pattern 1, the vertical force at the C-segments 1 and 2 is 123 MN in compression and 73 MN in tension, respectively. Due to its increased axial compressive force, C-segment 1 it stiffer and stronger; thus, it attracts much larger in-plane shear forces than C-segment 2. Another important remark pertains to the significant resistance contribution of flange 1, which is approximately 20% for both load patterns. The specific flange develops a significant axial compressive force at the lower stories, due to the combined effect of the gravity loads and of the diagonal compression field that partially transfers through the webs to the compression flange. The increase of axial compression results in an increase of the out-of-plane moment capacity and the out-of-plane shear force resistance up to the corresponding capacity (V_r). This level of resistance contribution from the flanges underlines the significance of accurately capturing the out-of-plane shear capacity in the flanges, as pursued in the present study and in the work by Alvarez.[35]

An important parameter to be investigated is the level of shear stress in the coupled web piers of the core wall. Hysteretic plots of the base story shear stress in each of the two web piers as a function of the drift ratio at the same story

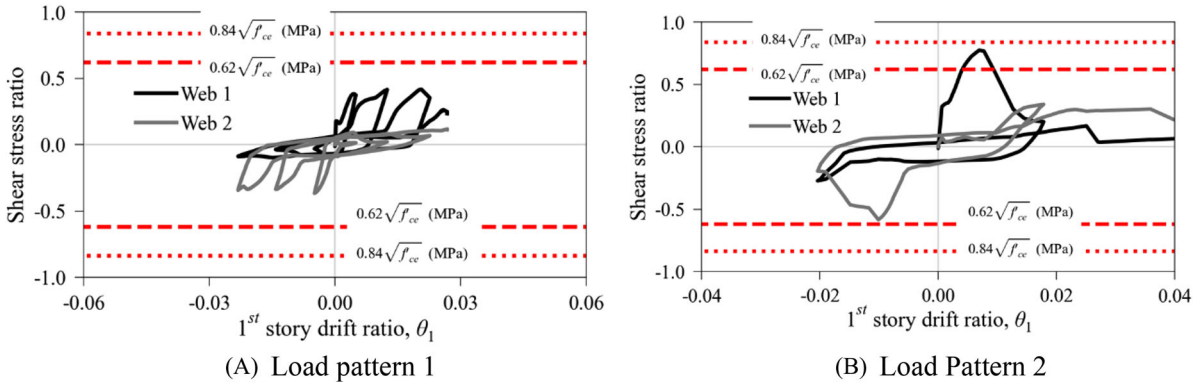

FIGURE 11 Average shear stress ratio of the bottom story web piers (X-direction) versus story drift ratio

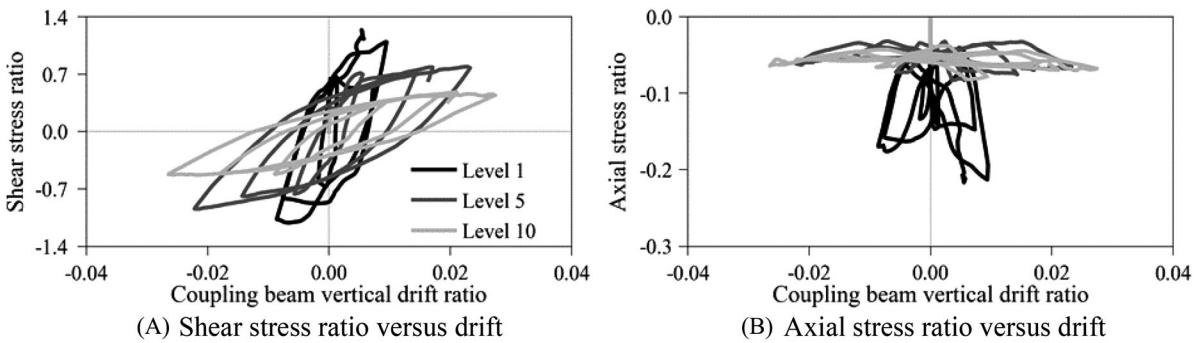

FIGURE 12 (A) Shear stress ratio of coupling beams; and (B) axial stress ratio of coupling beams of levels 1, 5, and 10 versus coupling beam drift ratio loading in the X-direction with load pattern 1

are presented in Figures 11A and 11B for load patterns 1 and 2, respectively. The figures also include the upper and lower limit values for the shear stresses in the specific wall per the design guidelines of the LATBSDC,[3] equal to $0.84\sqrt{f'_{ce}}$ MPa ($10.12\sqrt{f'_{ce}}$ psi) and $0.62\sqrt{f'_{ce}}$ MPa ($7.47\sqrt{f'_{ce}}$ psi), respectively. For each loading direction, the shear stress carried by the web pier in compression (leading web) is significantly higher than that in the other pier (following pier). The significant effect of the level of shear stress to the deformation capacity and nature of failure of the plastic hinge is evident. For load pattern 1, where the peak shear stress is $0.42\sqrt{f'_{ce}}$ MPa ($5.06\sqrt{f'_{ce}}$ psi), that is, 0.67 times the lower limit of LATBSDC, the base story develops a drift ratio of 2.1% before the occurrence of strength degradation. On the other hand, for load pattern 2 where the peak shear stress approaches the upper limit of LATBSDC, an abrupt strength degradation in the plastic hinge is initiated at a story drift ratio of 0.7%. The 0.7% first story drift capacity for load pattern 2 is significantly lower than the typical plastic hinge drift demands associated with the MCE_R level of response for this type of buildings.[46–48]

Figures 12A and 12B present the evolution of the shear stress ratios $V/(A_{cv}f'_{ce})$ and axial stress ratios $N/(A_g f'_{ce})$ in three coupling beams along the height of the building, as functions of the corresponding beam vertical drift ratios, obtained for the cyclic analysis using load pattern 1. The shear resistance of the coupling beam of the base story is much higher than that of the other stories. This is because of the much higher axial compressive force in the base story coupling beams, associated with kinematic interaction with the vertical wall piers. Specifically, inelastic deformations in the coupling beams create a tendency for axial elongation, which is restrained by the wall piers. This aspect of behavior is a major controlling factor for the evolution of damage and failure in the plastic hinge regions of coupled walls, as explained in more detail in Alvarez et al.[17] and Lu and Panagiotou.[20] Its accurate incorporation into a simulation necessitates models that account for the nonlinear flexure-shear-interaction in both the walls and coupling beams.

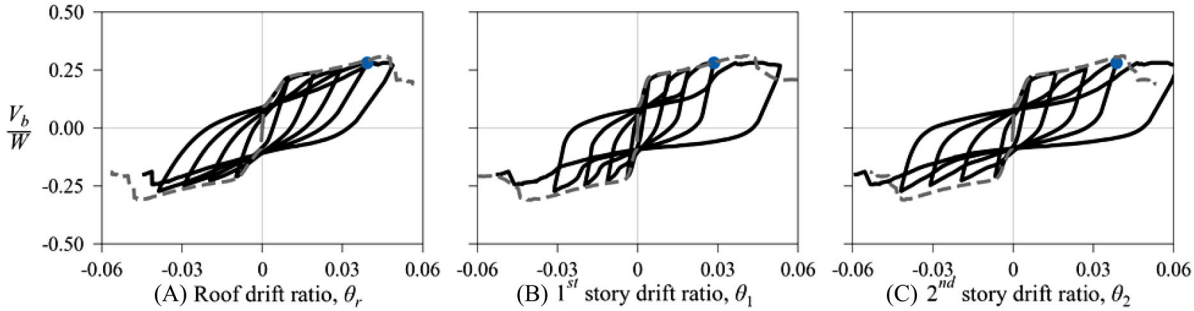

FIGURE 13 Hysteretic responses for loading along the Y-axis using load pattern 1

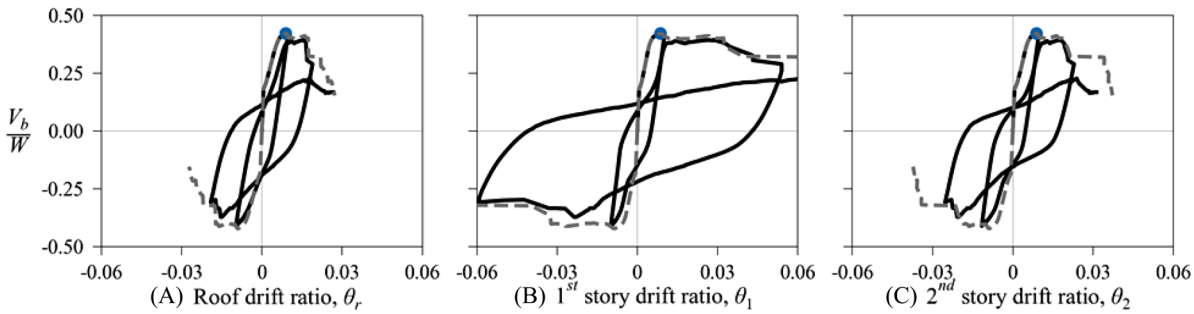

FIGURE 14 Hysteretic responses for loading along the Y-axis using load pattern 2

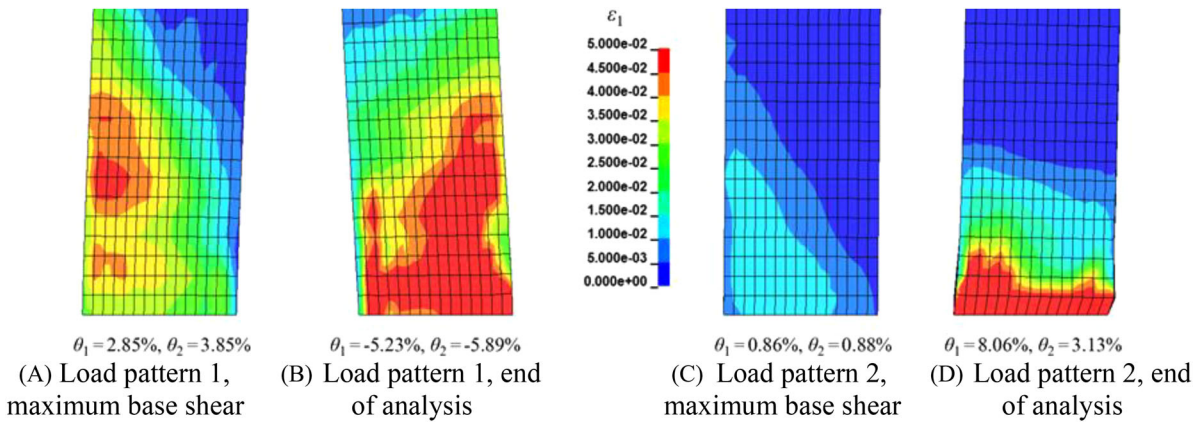

FIGURE 15 Deformed shape and max. principal strains (ε_1) of the core wall (Y-elevation) for Y-direction loading

8.2 | Results for loading in the Y-direction

The response for loading in the Y-direction is governed by the behavior of the two C-shaped walls. The obtained hysteretic curves for the building system, base story and second story obtained for load patterns 1 and 2 are presented in Figures 13 and 14, respectively. The figures also include the curves obtained for monotonic analyses, which provide reasonable match with the envelopes of the hysteretic curves in the pre-peak regime. Under cyclic loading, the maximum base shear force ratio V_b/W is 0.28 and 0.42 for load patterns 1 and 2, respectively. Strength degradation is initiated at a roof drift ratio of 4.1% for load pattern 1 and 1.6% for load pattern 2.

The maximum principal strain contours obtained at the instant of maximum base shear and at the end of the analysis for load pattern 1 are presented in Figures 15A and 15B, respectively. The behavior in the prepeak regime is flexure-dominated, with distributed deformations developing at the bottom three stories, as deduced from Figure 15A. The peak vertical tensile and compressive strain in the core wall up to the instant of peak base shear force are 0.050 and 0.023, respectively. Strength degradation is caused by rupture of the reinforcing bars at the base of the flange wall piers that are in tension. For load

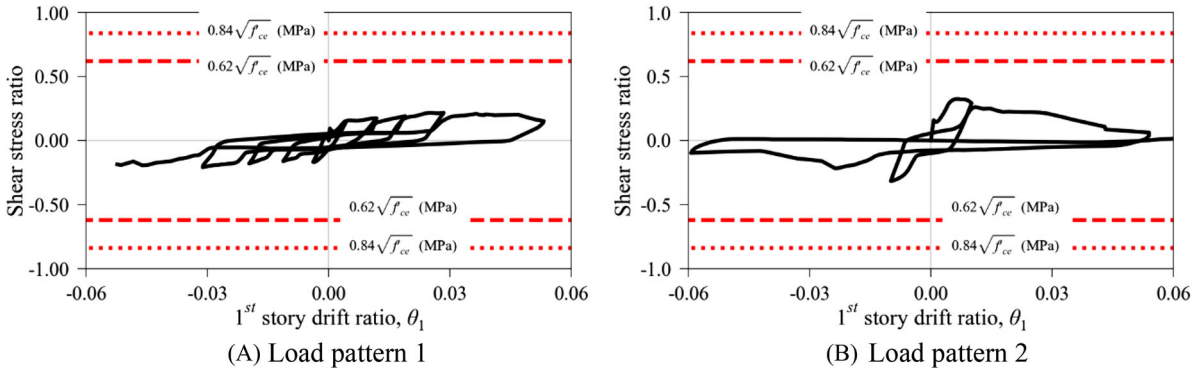

FIGURE 16 Average shear stress ratio of the base story core wall versus story drift ratio, for loading along the Y-direction

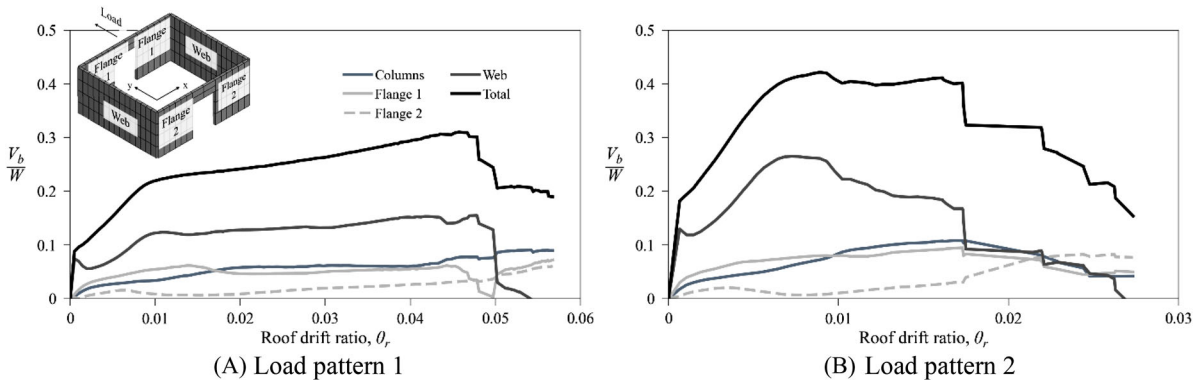

FIGURE 17 Contribution of various structural components to the lateral resistance of the structure, obtained for monotonic lateral loading along the Y-direction

pattern 2, the peak base shear is reached at 0.9% base story drift and the maximum principal strains in the bottom three stories at this instant is 0.013. At the next cycle, abrupt strength degradation initiates due to web crushing of the base story as deduced from Figure 15D.

The hysteretic plot of the wall web shear stress ratio, $V/(A_{cv}f'_{ce})$, at the base story, versus the corresponding story drift ratio, is presented in Figures 16A and 16B for the analyses with load patterns 1 and 2, respectively. The maximum shear stress obtained in the wall was $0.22\sqrt{f'_{ce}}$ MPa ($2.65\sqrt{f'_{ce}}$ psi) for load pattern 1 and $0.32\sqrt{f'_{ce}}$ MPa ($3.85\sqrt{f'_{ce}}$ psi) for load pattern 2. It is worth emphasizing that load pattern 2 led to a shear failure at a relatively low drift ratio, despite the fact that the recorded shear stress was about 50% of the lower limit of shear stress per LATBSDC. This is because the degradation is strongly related with horizontal inelastic strains which affect the tension strain normal to the diagonal compression field and hence the strength reduction of the diagonal compressive struts forming in the wall.

The evolution of the contribution of the various components to the lateral resistance of the system for monotonic analysis is shown in Figures 17A and 17B for load patterns 1 and 2, respectively. The majority of the lateral resistance is contributed by the web of the wall, followed by flange 1 (i.e., the flange that undergoes a compressive change in axial force under lateral displacements) and columns. The overall contribution of flange 2 to the lateral resistance is negligible. For load pattern 2 the web lateral resistance begins to degrade at a roof drift ratio of 0.7%. The system's lateral resistance does not degrade until reaching a drift ratio of 1.76%, because the loss of web resistance is counteracted by an increase in the lateral force contribution of flange 1 and columns. The decomposition of base shear resistance for cyclic loading with both patterns, summarized in Table 4, leads to similar observations as those made for loading in the X-direction.

9 | DISCUSSION AND DESIGN IMPLICATIONS

Table 5 summarizes key response parameters obtained from the cyclic analyses using the two load patterns, for both X- and Y-directions. The damage and failure in three out of four cases was dominated by nonlinear flexure-shear-interaction.

TABLE 4 Base shear contribution for loading along the Y-direction at the instant of maximum base shear

Base shear contribution	Load pattern 1	Load pattern 2
Web	63%	62%
Flange 1	17%	19%
Flange 2	8%	2%
Columns	12%	17%

TABLE 5 Summary of key response parameters for the four cyclic load cases

Response parameter	*Cyclic load case*			
	X load pattern 1	*Y load pattern 1*	*X load pattern 2*	*Y load pattern 2*
Wall failure mode	Shear failure of second story	Flexure failure of the flange	Shear failure of base story	Shear failure of base story
Peak V_b/W	0.30	0.28	0.47	0.42
Roof drift ratio at peak V_b	2.88%	3.91%	0.68%	0.89%
Base story drift ratio at peak V_b	2.07%	2.85%	0.69%	0.86%
Maximum wall vertical tension strain up to instant of peak V_b	0.042	0.050	0.011	0.013
Peak wall vertical compression strain up to instant of peak V_b	0.019	0.023	0.012	0.011
Maximum web horizontal strain up to instant of peak V_b	0.023	0.016	0.004	0.005
Peak shear stress of web	$0.42\sqrt{f'_{ce}}$	$0.22\sqrt{f'_{ce}}$	$0.78\sqrt{f'_{ce}}$	$0.32\sqrt{f'_{ce}}$

Specifically, the development of large inelastic deformations for the first load pattern in both-directions ultimately led to the occurrence of shear failure at large drift values, although the shear stresses computed for this load pattern were at least 32% lower than the limit value. On the other hand, the second load pattern in X-direction led to larger shear stresses in the wall webs than the first load pattern, which led to a significant reduction to the inelastic deformability of the core wall, quantitatively described by the roof drift ratio at the onset of lateral strength degradation. During actual nonlinear dynamic seismic response and depending on the relative contribution of higher modes, is expected the in-plane shear stresses to vary within the values obtained here for the two load patterns, affecting accordingly the deformation capacity of the building. Furthermore, in the direction of coupled wall piers (X-direction) capturing the critical coupling behavior requires the accurate representation of the connectivity of the coupling beams to the wall piers as also deduced from Figure 12. These observations stress the necessity of simulation tools such as the BTM, which can capture the inelastic shear-flexure interaction, for the seismic analysis of RC wall systems.

The out-of-plane behavior of the wall flanges is another relevant aspect not currently captured by most nonlinear analysis tools. Figure 18 presents the strain profile along the following flange (i.e., the flange subjected to upward axial forces due to the lateral displacements of the building), corresponding to the instant of peak base shear force. The profile is presented for two locations along the thickness of the flange, namely, at the middle of the thickness and at the surface of the flange having the largest tensile strains. The strain distributions are highly nonlinear, and the largest tensile strain values are obtained at the ends of the flange. The observed strain profiles cannot be obtained with RC wall panel elements commonly employed in PBSD practice because such elements do not model the nonlinear out-of-plane flexural behavior of flanges while they do not consider nonlinear-flexure-shear-interaction. Furthermore, the common practice of using one wall element for the entire length of a flange may further exacerbate the errors in the numerical representation of the wall behavior. For all cases considered herein, the two flanges (flange of the lead wall pier and flange of the following wall pier) had vastly different contributions to the lateral force resistance of the system. This important aspect of the behavior is not captured in current nonlinear analysis practice that models the out-of-plane behavior of flanges as linear elastic. The highly nonlinear out-of-plane behavior of the flanges can be observed in Figure 19 for load pattern 1 in the X-direction, which involves the formation of bands with localized out-of-plane flexural deformations in the flanges. The specific pattern is attributed to the fact that the end regions of the flange follow the in-plane displacements of the web piers that have failed in shear, while the flange regions away from the corners partially restrain this deformation.

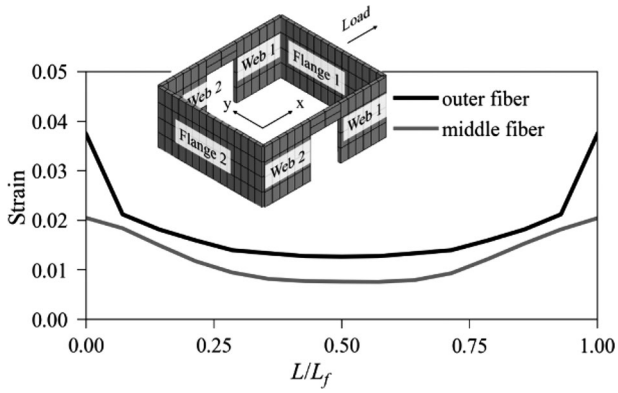

FIGURE 18 Vertical strain of the outer fiber and of the middle fiber at the base of the flange 2 along its length L at the instant of maximum base shear for loading pattern 1 along the X-direction

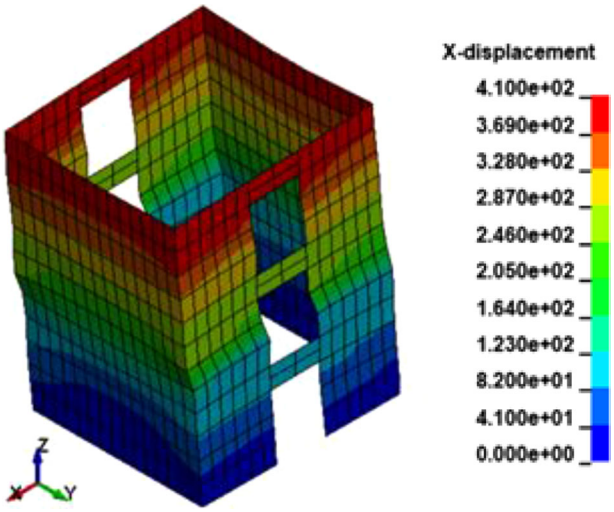

FIGURE 19 Deformed mesh of the bottom three levels at the end of the analysis for load pattern 1 along the X-direction with X-displacement contours (mm)

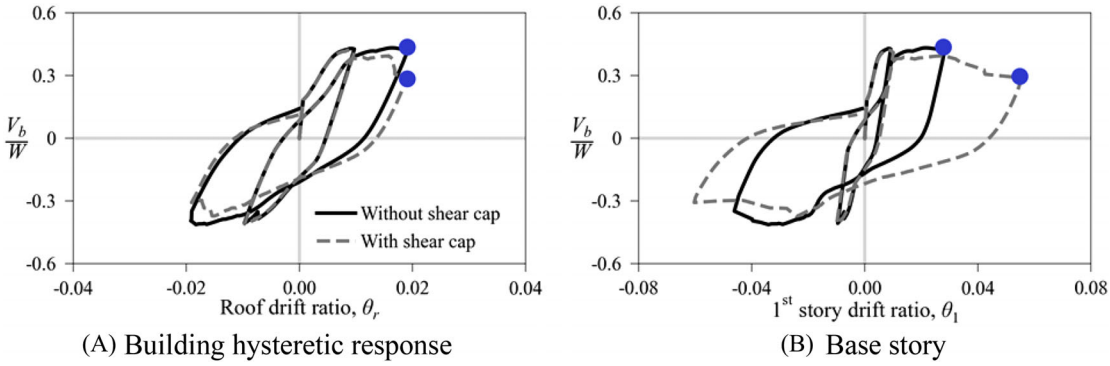

FIGURE 20 Hysteretic responses for loading along the Y-axis using load pattern 2 with and without out-of-plane shear cap capacity

Another aspect of the out-of-plane behavior of the flanges in the BTM is the impact of modeling the out-of-plane shear strength of flanges. To determine this impact the analysis for cyclic loading in the Y-direction with pattern 2 is repeated, this time without enforcing the cap to the out-of-plane shear strength of the flanges. The first two cycles of the hysteretic curves obtained with and without the cap are compared in Figure 20. Removing the cap increases the capability of the core wall to compensate for the strength degradation in the web, through the development of out-of-plane shear resistance in

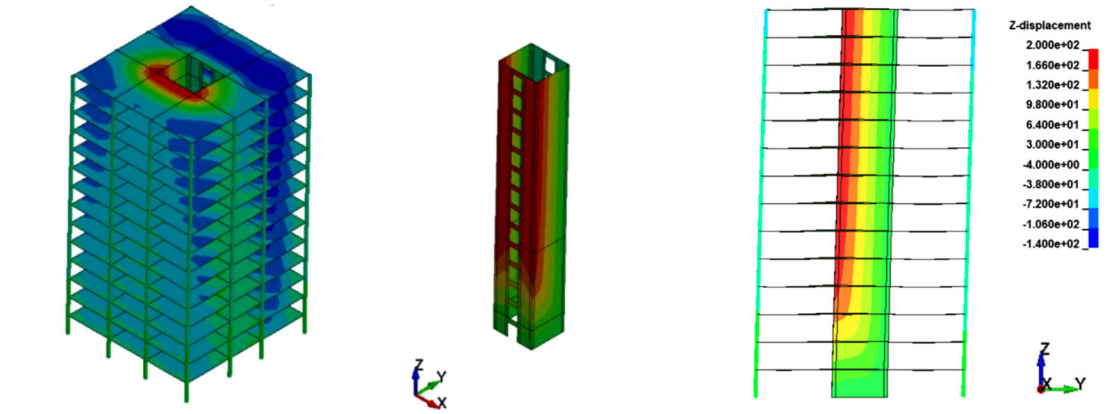

(A) Isometric view of building (B) Isometric core wall only (C) Elevation view core wall only

FIGURE 21 Vertical displacement contours at the instant of 3% roof interstory drift ratio for load pattern 1 along Y-direction

the flanges. As shown in Figure 20A, for the same roof drift the model with the cap has 33% less shear strength compared to the model without the cap. Accordingly, the post-degradation drift developed at the first story in the model with the cap is 1.92 times the first story drift of the model without the cap, as deduced from Figure 20B.

A discussion pertaining to the nonlinear system behavior and the coupling between the core wall, the slabs and the columns is also deemed necessary. Figure 21 shows the deformed shape of the building at a roof story drift ratio of 3%, for cyclic loading in the Y-direction with pattern 1. This is the cyclic load case that resulted in the largest vertical elongation (214 mm at the roof level) of the tension chord in the core wall. The axial elongation and rotation of the core wall imposes significant flexural deformations in the slab. The vertical displacement contours of Figure 21 an also indicate the formation of yield lines in the slabs associated with downwards vertical displacement. The slab coupling also affects the demands in the columns. The peak axial compression force at the base of the corner column is 26% higher than that corresponding to gravity loads. The slab coupling effect on the core wall is negligible, since it changes the vertical forces by less than 5%. For the specific building configuration considered herein, coupling most significantly affects the behavior of the slabs, and may have negative impact for the anticipated seismic performance. Specifically, the accumulation of inelastic deformations in the slabs can result in significant residual deformations and damage of the slabs, creating difficulties for the post-earthquake functional recovery. According to LATBSDC,[3] such system effects are typically not considered in nonlinear seismic analysis practice for slab span lengths exceeding 6 m.

The analyses using load pattern 1 indicated significant lateral design overstrength. Whereas the design base shear coefficient was $C_s = 0.13$, the peak base shear ratio obtained for loading with pattern 1 in the X- and Y-direction were 0.30 and 0.28, respectively. Hence, the computed overstrength factors were 2.31 for the X-direction and 2.15 for the Y-direction. This is because the flexural design (amount of vertical reinforcement) of the core wall was controlled by the load combination resulting in tension in the C-shape piers. In contrast, linear analysis of coupled core walls does not capture the significant variation of moment capacity between the compression and tension C-shape wall piers.

The shear stress values obtained in the analyses were generally lower than the limiting values used in PBSD guidelines such as those by the LATBSDC.[3] Only the analysis involving loading in the X-direction with pattern 2 resulted in shear stresses greater than the lower limit value prescribed by the LATBSDC.[3] The fact that the application of load pattern 2 in the Y-direction gave a shear failure at a relatively low roof drift value, even though the shear stresses were almost half the lower limit value in the LATBSDC[3] guidelines, indicates that the currently stipulated limit shear stress limits may not be adequate for ensuring a ductile seismic response. The thorough evaluation of the adequacy of these limits requires nonlinear dynamic analysis, which is beyond the scope of the present study, as well as shake-table tests of core wall buildings.

A final remark pertains to the fact that shear failure for load pattern 1 was obtained in the second story of the building. As mentioned in the previous section, this is attributed to the fact that load pattern 1 leads to practically identical values of shear force for the first and second story, but the design shear strength of the wall in the second story is lower than that of the bottom story. The lower shear resistance in the second story is attributed to the lack of ties outside the boundary elements of the wall section. A design recommendation based on these observations is to use out-of-plane ties for all vertical reinforcement in the plastic hinge region of core walls. Such ties enhance the out-of-plane shear resistance, while also providing anti-buckling behavior to all the vertical bars of the plastic hinge region. The use of ties for all vertical bars in the plastic hinge region is already applied by some engineers as best practice.

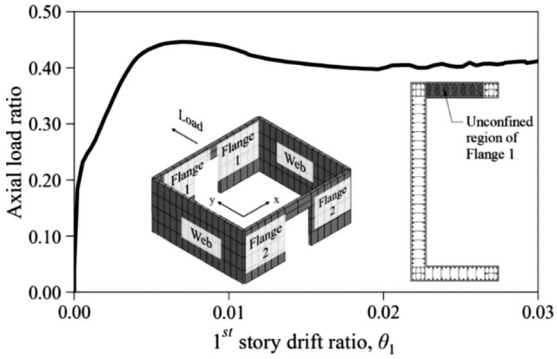

FIGURE 22 Axial load ratio of the unconfined region of Flange 1 versus first story drift ratio for load pattern 1 in the Y-direction

Despite its demonstrated capabilities, the BTM is currently characterized by several limitations. The current version of the BTM simulates the out-of-plane shear behavior in a simplistic fashion by limiting the out-of-plane shear capacity of a wall to a user's specified value as described previously. Since the out-of-plane nonlinear axial-flexure-shear-interaction is not considered in this study, the potential out-of-plane axial-shear failure cannot be captured. Figure 22 shows the axial load ratio versus 1st story drift ratio (up to 3% story drift ratio) of the unconfined region of Flange 1 (flange in compression) for the monotonic load pattern 1 in the Y direction. In this case, the unconfined region of Flange 1, resists vertical compression that corresponds to 45% axial load ratio. Under this high axial load, and in order to ensure an out-of-plane story drift ratio capacity of 3%, it is recommended that the entire section of the wall up to the story where the plastic hinge extends, to be detailed with confinement reinforcement consisting of closed hoops and ties similar to what is used here for Parts 1, 2, and 3. In addition, the present study did not consider the effects of skew or multiaxial loading that may reduce the deformation capacity of the building as shown in Panagiotou et al.[50] especially when only a small region near the corners of the core is confined.

Furthermore, for the confined regions the BTM does not consider explicitly the effect of axial compression and shear stresses interaction in the tension strain demands of the confinement reinforcement. Hence, the combined vertical compression and horizontal tension strain demands in confined regions should be evaluated accordingly, because this is what determines the rupture of confinement steel and hence the lateral capacity of the building for large drifts. A way to account partially for this type of behavior in the BTM is to use the concrete fiber removal option which enables the removal of the concrete part of the section, during the analysis, when a specific level of compression strain is exceeded. This technique was used by Deng et al.[19] to capture the experimentally tested behavior and failure of ductile RC walls including compression failures of confined boundaries. This technique is beyond the scope of this paper. Separate research studies are needed to develop appropriate multiaxial strain limits for confined boundary regions of RC walls.

The findings of the present study have been obtained on the basis of computational predictions and nonlinear static analyses for unidirectional loading. While static analyses facilitate the interpretation of the analytical results for a complex building system, actual earthquakes induce multidirectional dynamic excitations on the structure. An additional aspect, which was not present in the prototype structure considered herein but may be present in real-life multistory buildings, is the possibility for asymmetric in-plane arrangement of RC walls for a building, which may give rise to additional deformations due to torsional response. Future research, using nonlinear dynamic analyses, must supplement the present study to elucidate the additional impact and design implications of multiaxial nonlinear dynamic response, for example, dynamic amplification, bidirectional lateral loading, multimodal contribution, and torsional effects on buildings.

10 | CONCLUSIONS

This study investigated the seismic behavior of a modern 14-story RC core wall building hypothetically located in Los Angeles and designed per the current California Building Code[36] based on ASCE 7–16 and ACI 318–14. The investigation relied on nonlinear cyclic static analysis, using an enhanced version of the beam-truss-model (BTM) for the walls, coupling beams, and the slabs. The analyses were conducted for two different load patterns, that is, distributions of lateral forces along the height of the building, to study the effect of different levels of wall in-plane shear stresses on the seismic deformability and lateral capacity of the building system. For all cases considered, the response, damage pattern and failure were

governed by the nonlinear flexure-shear interaction in the wall piers. It was found that the deformation capacity of the building is significantly reduced for load patterns corresponding to relatively high shear stresses. Furthermore, the significant contribution of the compression flanges in overall story shear resistance is quantified together with the effect of modeling the out-of-plane shear capacity of flanges. Implications of this analytical case study on analysis and design following minimum code-requirements as well as performance-based-seismic-design guidelines are discussed. A major observation is that the shear stress limits currently stipulated in performance evaluation guidelines may not ensure an adequately ductile behavior of RC flanged coupled core wall buildings. Future studies using the BTM with nonlinear dynamic analyses and triaxial ground motions can be used to advance further the performance based seismic analysis of RC wall buildings.

DATA AVAILABILITY STATEMENT

Data available on request from the authors.

ORCID

Marios Mavros https://orcid.org/0000-0002-9538-8698
Ioannis Koutromanos https://orcid.org/0000-0002-3556-4258

REFERENCES

1. American Society of Civil Engineers. *Minimum Design Loads and Associated Criteria for Buildings and other Structures* : ASCE/SEI 7-16; 2017. https://ascelibrary.org/doi/book/10.1061/9780784414248
2. ACI. *ACI 318-14: Building Code Requirements for Reinforced Concrete*. ACI; 2014.
3. LATBSDC-20. *An Alternative Procedure for Seismic Analysis and Design of Tall Buildings Located in the Los Angeles Region*. 2020 Edition. Los Angeles Tall Buildings Structural Design Council; 2020.
4. Pacific Earthquake Engineering Center. *Guidelines for Performance-Based Seismic Design of Tall Buildings*. PEER Report; 2017.
5. Wallace JW, Segura CL, Tran TA, Shear design of structural walls. Proceedings, Los Angeles Tall Buildings Structural Design Council; 2013.
6. Barbachyn SM, Kurama YC, McGinnis MJ, Sause R. Testing and Behavior of Coupled Shear Wall Structure with Partially Post-Tensioned Coupling Beams. *ACI Structural Journal*. 2016;113(1). https://doi.org/10.14359/51687915
7. Beyer K, Dazio A, Priestley MJN. Quasi-static cyclic tests of two U-shaped reinforced concrete walls. *J Earthq Eng*. 2008;12:1023-1053. https://doi.org/10.1080/13632460802003272.
8. Thomsen JH, Wallace JW. Displacement-based design of Slender reinforced concrete structural walls—Experimental verification. *J Struct Eng*. 2004;130:618.
9. *Computers and Structures Inc*. PERFORM-3D User; 2011.
10. Oesterle RG, Fiorato AE, Johal LS, Carpenter JE, Russell HG. *Earthquake Resistant Structural Walls. Tests of Isolated Walls*. Skokie, IL: Portland Cement Association; 1976.
11. Oesterle RG, Fiorato AE, Johal LS, Carpenter JE, Russell HG, Corley WG. *Earthquake Resistant Structural Walls - Tests of Isolated Walls. Phase II*. Skokie, IL: Portland Cement Association; 1979.
12. Dazio A, Beyer K, Bachmann H. Quasi-static cyclic tests and plastic hinge analysis of RC structural walls. *Eng Struct*. 2009;31:1556-1571. https://doi.org/10.1016/j.engstruct.2009.02.018.
13. Panagiotou M, Restrepo JI, Conte JP. Shake-table test of a full-scale 7-story building slice. Phase I: rectangular wall. *J Struct Eng*. 2011;137:691-704. https://doi.org/10.1061/.(asce)st.1943-541x.0000332.
14. Panagiotou M, Restrepo JI, Schoettler M, Kim G. Nonlinear Cyclic Truss Model for reinforced concrete walls. *ACI Struct J*. 2012;109(2):205–214.
15. Lu Y, Panagiotou M. Three-Dimensional Cyclic Beam-Truss Model for Nonplanar Reinforced Concrete Walls. *Journal of Structural Engineering*. 2014;140(3):04013071. https://doi.org/10.1061/(asce)st.1943-541x.0000852
16. Lu Y, Panagiotou M, Earthquake damage-resistant tall buildings at near fault regions using base isolation and rocking core walls. Structures Congress 2015 - Proceedings of the 2015 Structures Congress; 2015. https://doi.org/10.1061/9780784479117.108
17. Alvarez R, Restrepo JI, Panagiotou M, Godínez SE. Analysis of reinforced concrete coupled structural walls via the Beam-Truss Model. *Eng Struct*. 2020;220:111005. https://doi.org/10.1016/j.engstruct.2020.111005.
18. Alvarez R, Restrepo JI, Panagiotou M, Santhakumar AR. Nonlinear cyclic Truss Model for analysis of reinforced concrete coupled structural walls. *Bull Earthq Eng*. 2019;17(12):6419-6436.
19. Deng X, Koutromanos I, Murcia-Delso J, Panagiotou M. Nonlinear truss models for strain-based seismic evaluation of planar RC walls. *Earthq Eng Struct Dyn*. 2021;50(11):2939-2960.
20. Lu Y, Panagiotou M. Three-dimensional beam–truss model for reinforced concrete walls and slabs – Part 2: modeling approach and validation for slabs and coupled walls. *Earthq Eng Struct Dyn*. 2016;45(11):1707–1724.
21. Palermo D, Vecchio FJ. Simulation of cyclically loaded concrete structures based on the Finite-Element Method. *J Struct Eng*. 2007;133:728-738.
22. Moharrami M, Koutromanos I. Finite element analysis of damage and failure of reinforced concrete members under earthquake loading. *Earthq Eng Struct Dyn*. 2017;46:2811-2829.

23. Dashti F, Dhakal RP, Pampanin S. Numerical Modeling of Rectangular Reinforced Concrete Structural Walls. *Journal of Structural Engineering*. 2017;143(6):04017031. https://doi.org/10.1061/(asce)st.1943-541x.0001729
24. Kolozvari K, Terzic V, Miller R, Saldana D. Assessment of dynamic behavior and seismic performance of a high-rise rc coupled wall building. *Eng Struct*. 2018;176:606-620.
25. Kolozvari K, Kalbasi K, Orakcal K, Massone LM, Wallace J. Shear–flexure-interaction models for planar and flanged reinforced concrete walls. *Bull Earthq Eng*. 2019;17:6391-6417.
26. Kolozvari K, Kalbasi K, Orakcal K, Wallace J. Three-dimensional model for nonlinear analysis of slender flanged reinforced concrete walls. *Eng Struct*. 2021;236:112105.
27. Vásquez JA, Jünemann R, de la Llera JC, Hube MA, Chacón MF. Three-dimensional nonlinear response history analyses for earthquake damage assessment: a reinforced concrete wall building case study. *Earthq Spectra*. 2021;37(1):235-261.
28. Gallardo JA, de la Llera JC, Santa María H, Chacón MF. Damage and sensitivity analysis of a reinforced concrete wall building during the 2010. *Chile Earthq Eng Struct*. 2021;240:112093.
29. Restrepo JI, Conte JP, Dunham RS, Parker D, Wiesner J, Dechent PAC. Detailed nonlinear FE pushover analysis of Alto Rio Building. 16th World Conference on Earthquake; 2017.
30. Maffei J, Bonelli P, Kelly D, et al. *Recommendations for Seismic Design of Reinforced Concrete Wall Buildings Based on Studies of the 2010 Maule, Chile Earthquake*. National Institute of Standards; 2014.
31. Bazant ZP, Planas J. *Fracture and Size Effect in Concrete and Other Quasibrittle Structures*. Routledge Taylor & Francis group; 1998.
32. Lu Y, Panagiotou M, Koutromanos I. Three-dimensional beam-truss model for reinforced concrete walls and slabs – Part 1: modeling approach, validation, and parametric study for individual reinforced concrete walls. *Earthq Eng Struct Dyn*. 2016;45:1495-1513. https://doi.org/10.1002/eqe.2719.
33. Zhang P, Restrepo JI, Conte JP, Ou J. Nonlinear finite element modeling and response analysis of the collapsed Alto Rio building in the 2010 Chile Maule earthquake. *The Structural Design of Tall and Special Buildings*. 2017;26(16):e1364. https://doi.org/10.1002/tal.1364
34. Álvarez R, Restrepo JI, Panagiotou M. RC wall plastic hinge out-of-plane buckling: analysis using the nonlinear Beam-Truss Model. *J Struct Eng*. 2020;146(12):04020274.
35. Alvarez R. *Seismic Response Verification of Reinforced Concrete Structural Wall Systems*. University of California San Diego; 2020. https://escholarship.org/uc/item/77k1b9k7
36. *California Building Code*. International Code Council; 2019.
37. *Computers and Structures Inc*. ETABS; 2018.
38. Koutromanos I, Farhadi M. FE-MultiPhys: a finite element program for nonlinear analysis of continua and structures. Tech Rep. 2018. https://doi.org/10.13140/RG.2.2.27375.38560
39. Panagiotou M, Koutromanos I, Advanced and practical seismic analysis of reinforced concrete walls and building systems using the BTM-shell methodology in the program FE-MultiPhys. Tech Rep. 2020. https://doi.org/10.13140/RG.2.2.27772.97924
40. Mander JB, Priestley MJN, Park R. Theoretical Stress-Strain Model for confined concrete. *J Struct Eng*. 1988;114(8):1804–1826.
41. The Modified Compression-Field Theory for Reinforced Concrete Elements Subjected to Shear. *ACI Journal Proceedings*. 1986;83(2). https://doi.org/10.14359/10416
42. Kim SH, Koutromanos I. Constitutive model for reinforcing steel under cyclic loading. *J Struct Eng*. 2016;142:04016133.
43. Dodd LL, Restrepo-Posada JI. Model for predicting cyclic behavior of reinforcing steel. *J Struct Eng*. 1995;121:433-445.
44. Girgin SC, Moharrami M, Koutromanos I. Nonlinear Beam-Based Modeling of RC Columns Including the Effect of Reinforcing-Bar Buckling and Rupture. *Earthquake Spectra*. 2018;34(3):1289–1309. https://doi.org/10.1193/063017eqs136m
45. Dhakal RP, Maekawa K. Path-dependent cyclic stress-strain relationship of reinforcing bar including buckling. *Eng Struct*. 2002;24:1383-1396.
46. Panagiotou M Seismic response of medium-rise and tall RC core-wall buildings at near-fault regions and simplified calculation of design demands. Annual Conference of Los Angeles Tall Buildings Structural Design Council; 2017.
47. Panagiotou M, Restrepo JI. Dual-plastic hinge design concept for reducing higher-mode effects on high-rise cantilever wall buildings. *Earthq Eng Struct Dyn*. 2009;38:1359-1380.
48. Calugaru V, Panagiotou M, Seismic response of 20-story base-isolated and fixed-base reinforced concrete structural wall buildings at a near-fault site. *Earthq Eng Struct Dyn*. 2014;43:927-948.
49. Panagiotou M, Restrepo JI. Displacement-based method of analysis for regular reinforced-concrete wall buildings: application to a full-scale 7-story building slice tested at UC–San Diego. *J Struct Eng*. 2011;137:677-690.
50. Panagiotou M, Koutromanos I & Mavros M et al. Nonlinear Beam-Truss Model (BTM) for seismic performance evaluation of reinforced concrete wall buildings. SEAOC Convention Proceedings, San Diego; 2021.

How to cite this article: Mavros M, Panagiotou M, Koutromanos I, Alvarez R, Restrepo JI. Seismic analysis of a modern 14-story reinforced concrete core wall building system using the BTM-shell methodology. *Earthquake Engng Struct Dyn*. 2022;51:1540–1562. https://doi.org/10.1002/eqe.3627